

Cu–Ni–PGE fertility of the Yoko-Dovyren layered massif (northern Transbaikalia, Russia): thermodynamic modeling of sulfide compositions in low mineralized dunite based on quantitative sulfide mineralogy

Alexey A. Ariskin^{1,2} · Evgeny V. Kislov³ · Leonid V. Danyushevsky⁴ · Georgy S. Nikolaev² · Marco L. Fiorentini⁵ · Sarah Gilbert⁴ · Karsten Goemann⁶ · Alexey Malyshev³

Received: 26 January 2015 / Accepted: 6 June 2016 / Published online: 22 June 2016
© Springer-Verlag Berlin Heidelberg 2016

Abstract The geology and major types of sulfide mineralization in the Yoko-Dovyren layered massif (northern Transbaikalia, Russia) are presented. This study focuses on the structure, mineralogy, and geochemistry of poorly mineralized plagiodunite and dunite in the lower part of the intrusion. Assuming these rocks contain key information on the timing of sulfide immiscibility in the original cumulate pile, we apply a novel approach which combines estimates of the

average sulfide compositions in each particular rock with thermodynamic modeling of the geochemistry of the original sulfide liquid. To approach the goal, an updated sulfide version of the COMAGMAT-5 model was used. Results of simulations of sulfide immiscibility in initially S-undersaturated olivine cumulates demonstrate a strong effect of the decreasing fraction of the silicate melt, due to crystallization of silicate and oxide minerals, on the composition of the intercumulus sulfide liquid. Comparison of the observed and modeled sulfide compositions indicates that the proposed modeling reproduces well the average concentrations of Cu, Cd, Ag, and Pd in natural sulfides. This suggests the sulfide control on the distribution of these elements in the rocks. Conversely, data for Pt and Au suggest that a significant portion of these elements could present in a native form, thus depleting the intercumulus sulfide melt at an early stage of crystallization.

Editorial handling: W. Maier

Electronic supplementary material The online version of this article (doi:10.1007/s00126-016-0666-8) contains supplementary material, which is available to authorized users.

✉ Alexey A. Ariskin
ariskin@rambler.ru

Evgeny V. Kislov
evg-kislov@ya.ru

¹ Faculty of Geology, Moscow State University, Leninskie Gory 1, 119234 Moscow, Russia

² Vernadsky Institute, Kosygin Str. 19, 119991 Moscow, Russia

³ Geological Institute, Sakhyanovoy Str., 6a, 670047 Ulan-Ude, Russia

⁴ CODES CoE and Earth Sciences, University of Tasmania, Private Bag 79, Hobart, TAS 7001, Australia

⁵ Centre for Exploration Targeting, School of Earth and Environment, ARC Centre of Excellence for Core to Crust Fluid Systems, The University of Western Australia, 35 Stirling Highway, 6009 Crawley Perth, WA, Australia

⁶ Central Science Laboratory, University of Tasmania, Private Bag 74, Hobart, TAS 7001, Australia

Keywords Yoko-Dovyren layered massif · Average sulfide composition · Mineralized dunite · COMAGMAT · Modeling S saturation · Precious metals

Introduction

A number of large layered intrusions and associated mafic–ultramafic complexes occur within the southern margin of the Siberian Craton. These complexes contain several different types of sulfide mineralization, including some economic Cu–Ni–platinum group element (PGE) deposits. Most of these complexes occur within the Precambrian folded sedimentary sequences at the margins of the Siberian Craton and have been collectively referred to as the East Siberian metallogenic province (Fig. 1; Polyakov and Izokh 2011;

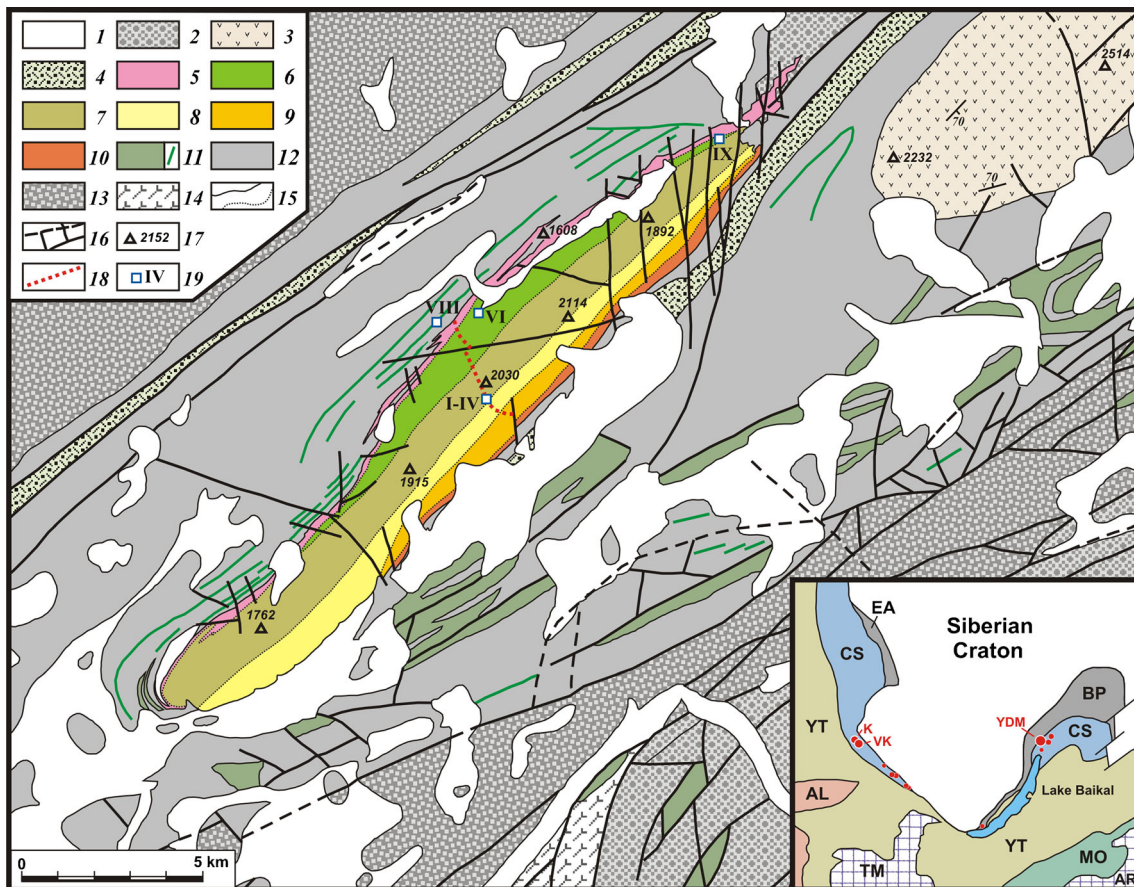


Fig. 1 Simplified geological map of the Dovyren area, modified after A.G. Krapivin (1975–1984) and A.G. Stepin (1991–1992). 1 Quaternary rocks (Middle–Late Quaternary). 2 Kholodninskaya Formation (Vendian–Early Cambrian). 3–11 Synnyr–Dovyren volcano–plutonic complex (Middle–Late Riphean): the Synnyr suite (3), the Inyaptuk suite (4), and the Dovyren intrusive complex (5–11): plagioclase lherzolite (5), dunite (6), troctolite (7), olivine gabbro (8), Ol gabbro and norite (9), quartz–pigeonite gabbro (10), and small bodies of mafic to ultramafic rocks (11). 12–13 Carbonate–terrigenous rocks: the Synnyr rift (12) and the Olokit trough (13). 14 Nyurundukansky metamorphic complex (Early Proterozoic). 15 Geological boundaries. 16 Faults. 17 Mount elevations. 18 Main sampled cross-section. 19 Outcrops of rocks shown in Fig. 5 (I–IV) and

Fig. 4: (VI) B, (VIII) C, and (IX) D. *Inset* shows Late Proterozoic intrusions of the southern margin of the Siberian Craton (East Siberian metallogenic province): *K* Kingash, *VK* Verkhni (Upper) Kingash, *YDM* Yoko–Dovyren massif, and other small mafic to ultramafic bodies hosting Cu–Ni–PGE deposits and sulfide ore occurrences (Polyakov et al. 2013). The geodynamic sketch is after Parfenov et al. (2010). Cratonal margins (Neoproterozoic and older basement): *BP* Baikal–Patom, *EA* East Angara. Tectonic Collages: *CS* Circum–Siberia (Proterozoic), *YT* Yenisey–Transbaikal (Vendian through Early Ordovician), *AL* Altay (Vendian through Ordovician), *MO* Mongol–Okhotsk (Devonian through Late Jurassic). Late Proterozoic and Cambrian superterrane: *AR* Argun–Idermeg, *TM* Tuva–Mongolia

Polyakov et al. 2013) based on the similarity of available age data (728 ± 3.4 Ma for the Yoko–Dovyren massif and 726 ± 28 Ma for the Upper Kingash; Ernst et al. 2012; Ariskin et al. 2013a, c). It was suggested that this mafic–ultramafic magmatism constitutes a Late Riphean large igneous province (LIP), which is contemporaneous with the ca. 725–715 Ma Franklin LIP in northern Canada and western Greenland, associated with the breakup of Rodinia (Heaman et al. 1992; Jowitt and Ernst 2013).

The Cu–Ni sulfides within the Yoko–Dovyren massif (YDM) were discovered in 1959 (Kislov 2010, 2013). In this study, we provide detailed information on the Cu–Ni–PGE mineralization of the YDM, focusing on the spatial and genetic relationships between Ni-rich sulfides observed in olivine

cumulates near the bottom of the YDM and the PGE-rich sulfide-poor anorthosite in the mafic part of the intrusion (Kislov 1998; Ariskin et al. 2013a). As the primitive olivine cumulates record the earliest stages of sulfide immiscibility in the YDM magma chamber, we perform a series of COMAGMAT-5 calculations on their bulk rock compositions to determine the timing of sulfide immiscibility and the sulfide geochemistry in the original cumulate pile (Ariskin and Danyushevsky 2014). These results provide new constraints on the behavior of base metals and highly chalcophile elements during the crystallization of layered mafic–ultramafic complexes.

This study is based on a subset from a collection assembled in 2006–2014, which includes over 1250 samples

representing three complete cross-sections through the YDM, several sections through associated volcanic sequences, sections across several mafic–ultramafic sills, and samples of Cu–Ni sulfide ores, Ni-rich disseminated mineralization, and PGE-rich anorthosite.

The Dovyren intrusive complex

Regional geology

The Dovyren intrusive complex includes the YDM, mafic to ultramafic sills underlying the YDM, and associated dikes of gabbronorite both below and above the massif (Grudinina 1963; Gurulev 1965; Yaroshevsky et al. 1982; Konnikov 1986). Spatially and temporally, these intrusive rocks are associated with low-Ti and high-Ti volcanic sequences of the Synnyr ridge (Manuilova and Zarubin 1981; Konnikov et al. 1988; Fig. 1). The entire association is referred to as the Synnyr–Dovyren magmatic complex emplaced at 728 ± 3.4 Ma (Ariskin et al. 2009a, 2013c).

The YDM itself is located ~60 km NE of Lake Baikal and forms a 26-km-long ridge. The massif is a lens-shaped body ~3.5 km thick in its center. The YDM is concordant with the host rocks, which comprise an Upper Riphean carbonate–terigenous sedimentary sequence mostly made up of black shales. This sequence is part of the ~400-km-long Olokit-Bodaibo trough along the southern margin of the Siberian Craton (Konnikov et al. 1999; Rytsek et al. 2002).

General structure of the Yoko-Dovyren massif

Because the dip of the layering of the Synnyr–Dovyren complex is nearly vertical, it was possible to collect samples from the base of the YDM to its upper contact. In the central part, the YDM is subdivided into three major units: the lower ultramafic section (~2100 m), the middle gabbroic section (~1050 m), and the uppermost ~220-m-thick unit that contains the most fractionated gabbro and gabbronorite (Yaroshevsky et al. 1982; Konnikov 1986). In the central part of the YDM, the lower ultramafic section is poorly mineralized (<0.1 wt% S), as opposed to the NE and SE terminations of the YDM and the sills in the floor, which are mineralized (up to 6–7 wt% S; Kislov 1998).

In detail, the YDM (Fig. 2) is subdivided into the lower chilled unit (<30 m), basal plagioperidotite (100–150 m), plagiodunite (up to 80 m), “non-contaminated” and “contaminated” dunite (~970 m), troctolite (~950 m), olivine gabbro (~450 m), a ~600-m-thick zone of interbedded olivine norite and gabbronorite, and the near-roof sequence of pigeonite gabbro and gabbronorite. Numerous schlieren and veins of quartz granophyre are common both just below and within the uppermost unit. Fine-

grained gabbronorite, containing up to 9 wt% MgO, forms the upper contact of the intrusion (Kislov 1998).

Below, we describe in more detail the basal rocks of the YDM, from the lower chilled rocks to the plagiodunite and the lowest dunite (Fig. 2). These rocks record information on the nature of the parental magmas of the Yoko-Dovyren massif (Ariskin et al. 2015) and contain a horizon of poorly mineralized sulfide-bearing rocks.

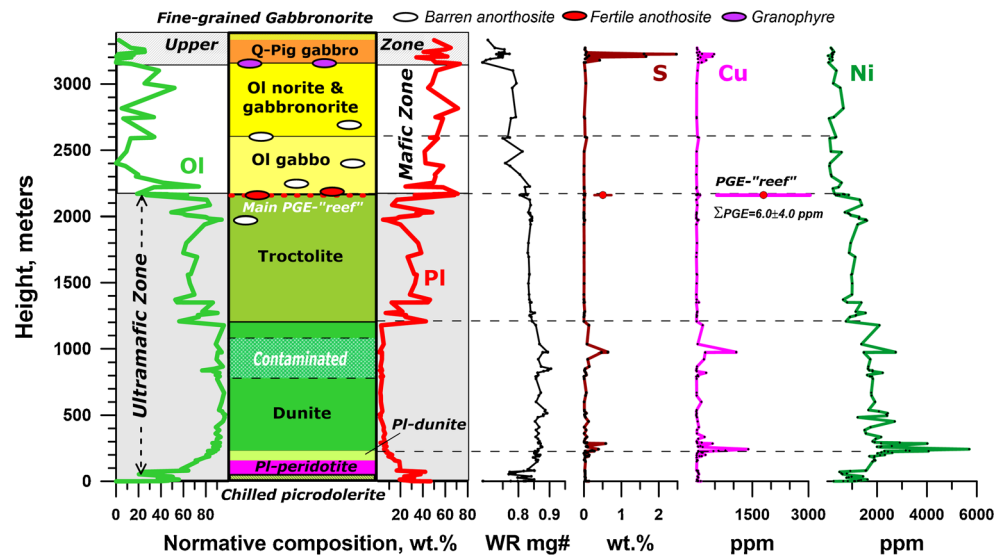
Chilled rocks

Similar to the Basal Series of the Stillwater Complex (Keays et al. 2011) and the chilled sequence of the eastern Bushveld Complex (Wilson 2012), the lower contact of the Yoko-Dovyren massif comprises a complex package of olivine-rich, orthopyroxene-bearing cumulates. Based on several outcrops of the lower contact in the central part of the YDM, the section begins with an ~0.5- to 1-m-thick chilled sequence composed of fine-grained sub-ophitic gabbronorite (“ophitic gabbro” or “picrobasalt”; Gurulev 1983). These rocks are composed of aggregates of altered plagioclase, pyroxene, bronze biotite to brown phlogopite, rare resorbed olivine, and idiomorphic chromite and apatite.

The chilled rock is replaced up the section by “picrodolerite” (Online Resource 2), which constitutes a 5- to 15-m-thick sequence that contains variable amounts of cumulus olivine. Texturally, the transition from the chilled gabbronorite to high-Mg picrodolerite is characterized by the appearance of subhedral and more abundant olivine grains (0.4–2 mm in size), transforming the chilled texture of the former into the porphyric texture of the latter. The large amount of thin plagioclase laths within picrodolerites results in the ophitic texture of the groundmass (Fig. 3, DV30-1). Olivine composition in the picrodolerite changes from Fo71-77 in the olivine-poor varieties to Fo81-83 in the olivine-rich rocks. Orthopyroxene (Mg#71–84; Mg# is the molar ratio MgO/(MgO+FeO)) is common, generally showing reaction relationships with olivine, whereas chromite (Cr#66±4; Mg#25±4; Cr# is the atomic ratio Cr/(Cr+Al)) is abundant as inclusions in olivine and pyroxene (Kislov 1998).

The picrodolerite displays a sequential change toward more magnesian olivine orthocumulates containing up to 20–25 wt% MgO. Their textural features are also indicative of fast cooling of an olivine-laden parental magma (Ariskin et al. 2009a). At a distance of 5–15 m from the lower contact, even more magnesian rocks are observed (25–30 % MgO), which can be referred to as olivine–chromite mesocumulates. However, less magnesian rocks (<20 % MgO) are still present in the upper parts of this sequence.

Fig. 2 Internal structure of the Yoko-Dovyren massif along a typical cross-section through its central part (Fig. 1; Ariskin et al. 2015). As most Dovyren rocks represent low-porosity cumulates and adcumulates, the normative proportions of olivine and plagioclase were calculated assuming low $Fe^{3+}/\Sigma Fe = 0.05$ in the rocks. S and Cu concentrations are from this study, with the exception of five samples of a fertile anorthosite from PGE Reef I, which were used to calculate their average S and Cu contents (Tolstykh et al. 2008)



Plagioperidotite

The high-magnesian orthocumulates (~17–25 % MgO) and mesocumulates (25–30 % MgO) display a range of textures from olivine-phyric rocks with a dolerite-like groundmass to poikilitic rocks with subhedral plagioclase and large grains of poikilitic pyroxenes surrounding and resorbing the original cumulus olivine (Fig. 3, see 07DV132-7 and 07DV132-9). Based on their petrographic features, the latter rocks are commonly classified as “plagioperidotite” or “plagioclase lherzolite” (Konnikov 1986; Kislov 1998). The textural variability between compositionally similar picrodolerite and

plagioperidotite argues for differences in the rate of cooling of the original olivine-laden magmas, with a fine-grained texture of faster cooling closer to the contact (compare the textures of DV30-1 and 07DV132-9 in Fig. 3).

In the center of the YDM, the transition from high-Mg picrodolerite to the overlying plagioperidotite occurs in the interval from 3–5 to 10–15 m from the lower contact. The plagioperidotite makes up a 100- to 150-m-thick unit. Highly serpentinized varieties of these rocks are readily mapped by their black color and enrichment in phlogopite. In less altered rocks, this transition is recorded in a gradual inward decrease in phlogopite and olivine (up to

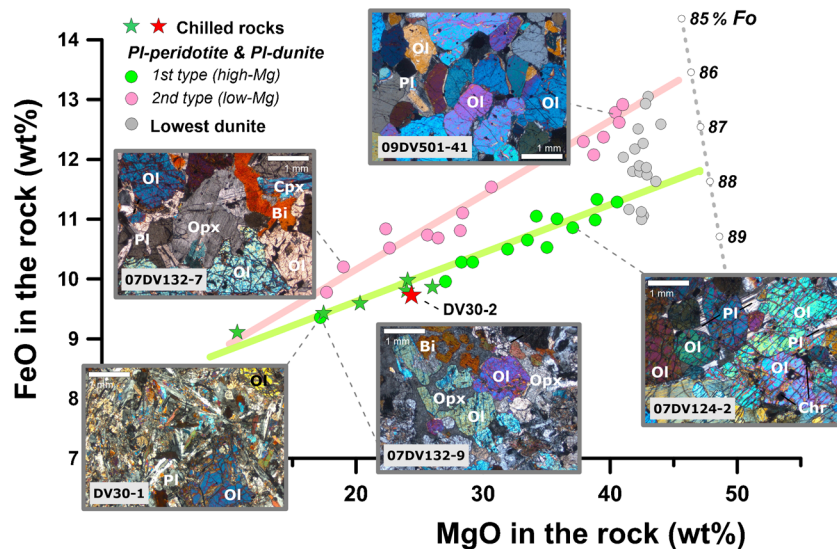


Fig. 3 FeO–MgO diagram for mafic to ultramafic rocks in the basal units of the Yoko-Dovyren massif. Two distinct trends are identified: the *high-Mg* (Fo88) and *low-Mg* (Fo86) trends, both consistent with Ol-laden parental magmas differing in Mg# of their initial transporting melts. DV30-1: Ol-phyric picrodolerite ($h \sim 0.5$ m from the lower contact, first

type); 07DV132-7: plagioperidotite ($h = 61$ m, second type); 07DV132-9: plagioperidotite ($h = 72$ m, first type); 07DV124-2: PI-dunite ($h = 162$ m, first type); 09DV501-41: transitional PI-dunite ($h = 217$ m, second type). DV30-2 is picrodolerite used for thermodynamic modeling of the composition of the immiscible sulfide liquid

50–60 vol%), accompanied by a transition from ophitic through to poikilitic and hypidiomorphic texture of the groundmass (Ariskin et al. 2015).

On the FeO–MgO diagram (Fig. 3), the whole-rock compositions of all chilled rocks and approximately half of the sampled plagioperidotite (Online Resource 2) follow a trend pointing toward olivine ~Fo88. The remaining points form a trend of more Fe-rich compositions, which point toward olivine ~Fo86. For a given MgO content of the rock, the plagioperidotite of the high-Fo trend contains more magnesian olivine with a higher NiO content compared to the plagioperidotite from the low-Fo trend. Both types of plagioperidotite are concordant, forming sub-layers with a thickness of 5–25 m, none of which display quenched textures.

The heterogeneous nature of the basal zone may reflect the crystallization of two types of olivine-laden parental magmas. Accordingly, the magmas contained olivine phenocrysts of different compositions (either Fo86 or Fo88), most likely due to different temperatures of emplacement rather than to different geochemical types of parental magmas. These two parental magmas were emplaced simultaneously during the early stages of formation of the YDM. First results of numerical modeling of crystallization of the high-Fo type of parental magmas using the COMAGMAT model have shown that these parental magmas were characterized by temperatures below 1300 °C, MgO contents in the melt <11 wt%, and contained olivine in equilibrium with the melt with compositions of Fo87.5–88 (Ariskin et al. 2009c).

Plagiodunite and the lowest dunite

Plagiodunite makes up a 60- to 80-m-thick horizon that overlies the plagioperidotite zone and may be considered as a transitional zone toward the overlying dunite (Ariskin et al. 2015). The transition from plagioperidotite and plagiodunite occurs as a 10- to 30-m zone where the amount of orthopyroxene oikocrysts and phlogopite decreases upwards. Chemically, it is correlated with a depletion in Ti, K, P, and other incompatible trace elements, reflecting the continued upward decrease in the amount of intercumulus material (composed mainly of plagioclase) in the olivine cumulates (Fig. 3, see 07DV124-2). This process results in higher MgO contents of the plagiodunite compared to the plagioperidotite (Online Resource 2 and Fig. 3).

The transition from plagiodunite to the adcumulate dunite (Fig. 3, see 09DV501-41) is also gradual. Both interbedding poikilitic plagiodunite and hypidiomorphic adcumulate dunite are observed over a zone of 20–40 m. In this transitional zone and in the lowest dunite, olivine composition ranges within Fo85–87. These rocks are much less altered than the underlying plagioperidotite, with only occasional serpentinization developed along fractures in olivine. Within the transitional

zone, an upward increase in bulk S is observed (from <0.01 to 0.28 wt%), which is correlated with the increased amount of disseminated orthomagmatic pentlandite-rich sulfides.

Sulfide occurrences and Cu–Ni–PGE fertility of Dovyren

Sulfide occurrences within the YDM range from widespread disseminated sulfides to net-textured and massive pyrrhotite-rich ores at the lower contact and within the underlying ultramafic sills (Kislov 1998, 2013; Fig. 4). Additionally, sulfide-poor PGE-rich mineralization is present within anorthosite near the transition from troctolite to olivine gabbro (Distler and Stepin 1993; Konnikov et al. 1994, 2000; Kislov et al. 1995; Orsoev et al. 2003), as shown in Fig. 5.

Cu–Ni syngenetic mineralization

The syngenetic mineralization includes disseminated sulfides to “impregnation ores” (locally net-textured) that are irregularly distributed throughout the entire massif and associated mafic to ultramafic sills (Kislov 1998). The most sulfide-rich occurrences (up to 30 % sulfides) are associated with plagioperidotite below the bottom of the intrusion in the underlying ultramafic sills (Fig. 1). Outcrops of the syngenetic sulfide ore bodies may be traced continuously in parallel to the lower contact of the YDM for ~1700 m. Their orientation matches the strike and dip of both the sills and the YDM (Kislov 1998). The width of the ore lenses varies from 8 to 25 m, locally reaching 80 m. Pyrrhotite (up to 85–95 %) is the main sulfide.

Poorly mineralized rocks with fine-grained disseminated sulfides also make up an ~150-m horizon within the transition zone from plagiodunite to the adcumulate dunite (Kislov et al. 1995; Figs. 2 and 6). Pentlandite-rich sulfides are predominant in these rocks. Another area occurs in the upper part of the dunite zone of the YDM, where magnesian skarns developed in place of assimilated carbonates (Konnikov et al. 2000; Fig. 2).

The orthomagmatic mineralization in gabbronorite is subdivided into two varieties. Rocks relatively rich in disseminated sulfides are usually localized in areas where dikes of a granophyric gabbronorite and/or gabbro-pegmatite cut the basal plagioperidotite and underlying ultramafic sills. Additionally, a distinct horizon of pyrrhotite-rich sulfide-bearing gabbronorite exists near the roof of the YDM, where the mineralized rocks contain up to 3 wt% S (Fig. 2). Within these two locations, mineralization occurs as finely disseminated sulfides (0.5–3 mm) which locally form large irregular blebs up to 20 mm in size. Similar to the ultramafic rocks with a higher proportion of sulfides, pyrrhotite is the predominant phase. However, the amount of chalcopyrite is markedly higher in gabbronorite.

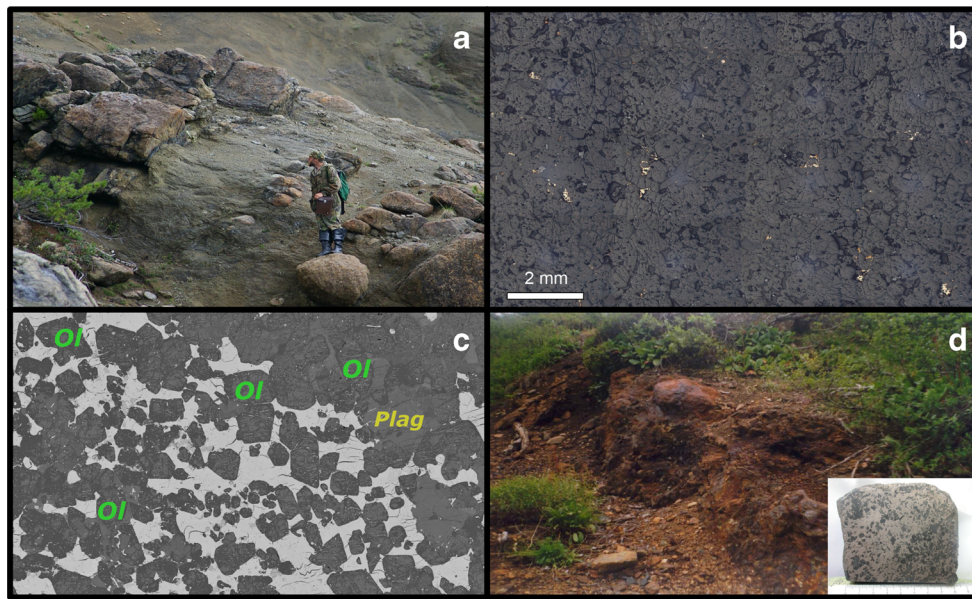


Fig. 4 Main types of Cu–Ni mineralization of the Yoko-Dovyren massif. **a** Outcrops of almost unaltered dunite in the lower part of YDM. **b** Sulfide-poor mineralization in the Dovyren dunite (sample 07DV124-5, 0.28 wt% S). In addition to disseminated sulfides, the interstices between olivine crystals are filled with plagioclase, rare clinopyroxene, and phlogopite. **c** BSE image of the net-textured sulfides from a sill

underneath the YDM in its central part (sample 07DV107-1, 12 wt% S). **d** Lode of a massive Po-rich sulfide ore. *Inset* shows polished slab of massive sulfides (the Ozernyi prospect in NE termination of YDM; pictures by D.A. Orsoev, Geological Institute in Ulan-Ude, Buryatia, Russia)

Cu–Ni epigenetic mineralization

The epigenetic mineralization is represented by massive (Fig. 4d) and vein-like brecciated ores, commonly occurring within the zone of disseminated sulfide ores. The first and the largest sulfide lode was discovered in 1959 at the NE contact of the YDM (the Ozernyi prospect; Denisova

1961). It extends along the base of the massif for a distance of 650 m and is 0.7–1.0 m wide. Lodes of smaller sizes (15–50 m long and 0.2–1.5 m thick) are confined to fractures demarcated by sills and dikes of gabbro (Kislov 2010). Sulfide-rich veins dip near vertically extending to depths of >500 m. The massive ores consist of pyrrhotite and contain minor amounts of troilite,

Fig. 5 Examples of veins and schlieren of mineralized and barren anorthosites from the Main Reef (Reef I) of the Yoko-Dovyren massif. **a** Thick vein of anorthosite. **b** Schlieren of anorthosite. **c** Contact of the anorthositic schlieren with olivine gabbro. **d** Sulfide-rich area surrounded by altered plagioclase. **e** BSE image of interstitial pentlandite associated with a complex grain including native Au–Cu–Pd alloys and Pt–Pd–Pb (Bi) tellurides, Reef I (Fig. 2)

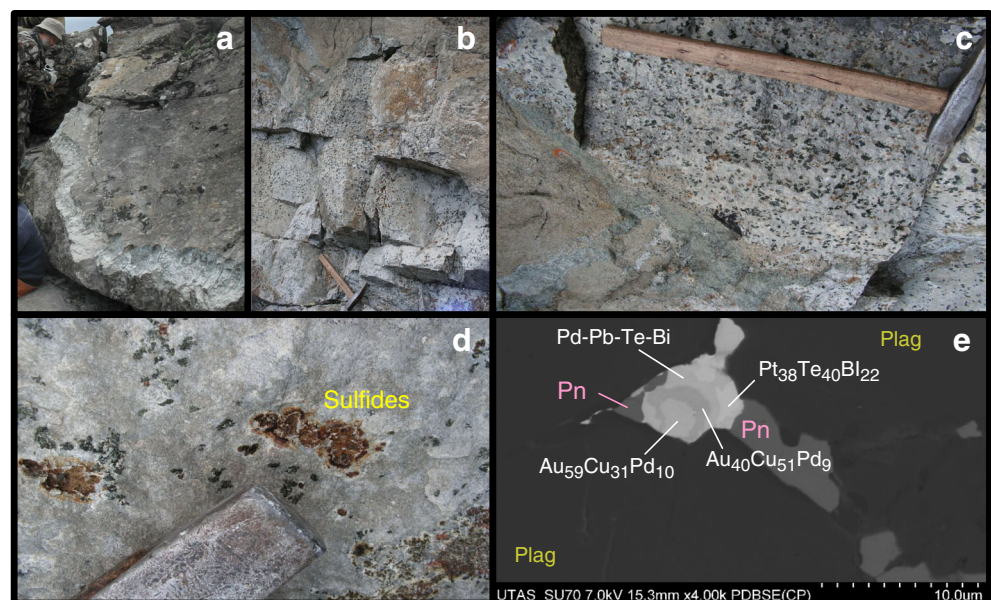
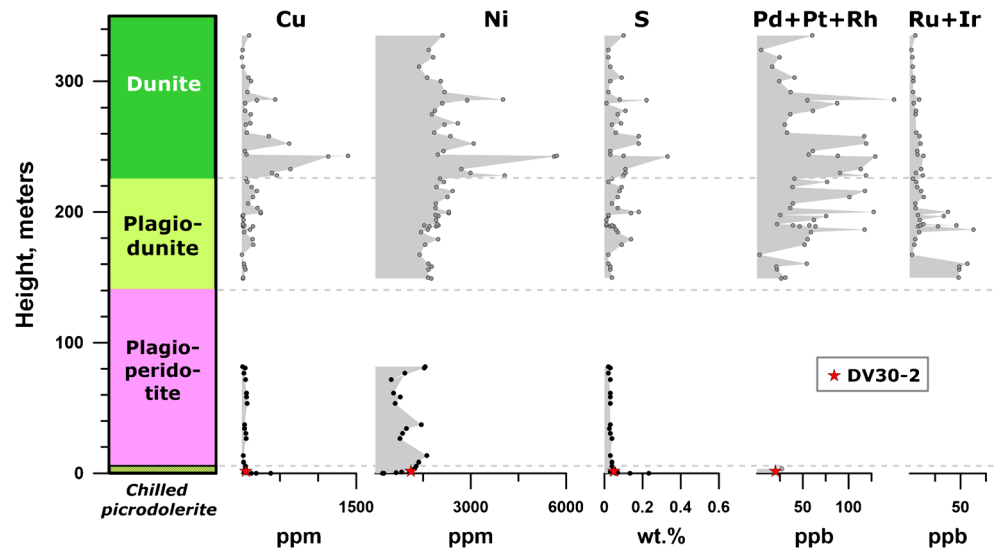


Fig. 6 Contents of base metals, S, and PGE in the rocks plotted against their position in the lower zones of the Dovyren intrusion (see the main cross-section in Fig. 2). DV30-2 is picrodolerite from the chilled zone of YDM (Fig. 3). The lower peak in IPGE represents a chromium-rich horizon



pentlandite (7–25 vol%), and chalcopyrite (0.1–6 vol%). The other minor minerals are cubanite, ilmenite, magnetite, and pyrite; occasionally, mackinawite, titanomagnetite, sphalerite, and molybdenite. Average contents of base metals in the sulfide ores are given in Table 1. The concentrations of precious metals by different analytical techniques during 1962–1993 are highly variable, with Pd ranging from 0.1 to 0.9 ppm, Pt 0.01–0.26 ppm, and Au 0.01–0.1 ppm (Tolstykh et al. 2008).

The vein-like brecciated ores are relatively rich in PGE: commonly 0.4–1.5 ppm Pd, 0.1–0.2 ppm Pt, and up to 0.14 ppm Au (Tolstykh et al. 2008). Limited data for the massive lode indicate 0.82 ppm for Pd, but much lower Pt contents of 0.03 ppm (Distler and Stepin 1993). The higher content of Pd over Pt is distinctive for the Cu–Ni sulfides of the Baikal Deposit. Mineralogical studies have identified a diversity of platinum group minerals (PGMs), including sperrylite PtAs₂, geversite PtSb₂, mertieite-I Pd₅(Sb,As)₂, naldrettite Pd₂Sb, and electrum. The size of the grains,

recovered by hydroseparation of dense mineral phases, ranges from 9 to 63 μm (Rudashevsky et al. 2003).

PGE-rich sulfide-poor mineralization

A zone of the PGE-rich sulfide-poor mineralization has been traced within the gabbroic part of the massif along its strike for over 20 km (Kislov 1998). The main PGE-rich horizon (the Main Reef, or Reef I) is located within the transition zone from the rhythmic layered troctolite to barren and poorly mineralized olivine gabbro and leucogabbro. This highly heterogeneous zone has a variable thickness (150–200 m) along strike and is composed of concordant veins and lenses of coarse-grained and taxitic troctolite and gabbroic rocks, including sulfide-poor anorthosite (Orsoev et al. 2003; Tolstykh et al. 2008), as shown in Fig. 5. The sulfide-poor anorthosite forms large schlieren and lens-like bodies commonly surrounded by gabbro-pegmatite. Anorthositic bodies (differing in lithology from plagioclase-rich leucogabbro and

Table 1 Average contents of base metals in Cu–Ni sulfide ores and mineralized rocks of the Yoko-Dovyren massif (after Kislov 1998; Tolstykh et al. 2008)

Types of sulfide occurrences	n	Concentrations (wt%)			
		S	Ni	Co	Cu
Poorly mineralized Pl-peridotites	10	0.62	0.122	0.014	0.025
Disseminated sulfides to relatively poor impregnation ores in Pl-peridotites	16	1.72	0.137	0.017	0.055
Rich impregnation ores in Pl-peridotites	11	9.35	0.911	0.055	0.345
Cu-rich impregnation to vein-like ore in gabbronoritic diabases	1	14.24	1.27	0.032	4.6
More common impregnation to vein-like ores in gabbronoritic diabases	15	9.21	0.684	0.05	0.49
Lode to vein massive and brecciated ores	13	22.01	1.82	0.101	0.475

n is the number of assays

gabbronorite to almost pure anorthosite) are usually a few centimeters to 1 m thick and extend for 2–5 m along strike of the massif (rarely >40 m long), forming a discontinuous sulfide-poor mineralized zone. The second PGE-rich horizon (Reef II) lies ~600 m above Reef I within the transition zone from Ol-gabbro to gabbronorite (Konnikov et al. 2000).

Despite the sulfide-poor character of Reef I mineralization, the amount of PGE-bearing sulfides in the anorthosite may locally reach up to 3–5 vol%. The sulfide assemblages are Cu-rich, including chalcopyrite, cubanite, bornite, and, in rare cases, talnakhite and godlevskite (Konnikov et al. 2000). Pentlandite and pyrrhotite are minor phases (both <15–20 vol%). Using hydroseparation of a finely crushed 6 kg assay of sulfide-poor Reef I anorthosite (26 % Al₂O₃, 1.29 ppm Pt, 1.05 ppm Pd), 70 PGM grains, 7 grains of electrum, and 3 grains of Ag minerals (argentite, stephanite Ag₅SbS₄, and amalgam AgHg) were recovered (Rudashevsky et al. 2003; Orsoev et al. 2003). Fourteen different PGMs ranged in size from 4 to 62 μm (Tolstykh et al. 2008), including moncheite (*n* = 22), potarite PdHg (*n* = 17), and tetraferroplatinum (*n* = 15). Minor PGMs included kotulskite Pd(Te,Bi,Pb), sobolevskite Pd(Bi,Te), and nine stibnides, stannides, and plumbides. Only one ~11-μm-sized grain of sperrylite was found.

Due to the irregular distribution of sulfides in the PGE horizon, the concentration of precious metals in the mineralized rocks is heterogeneous. The total contents of PGE+Au vary in the range 0.3–12.1 ppm at 0.006–0.710 wt% Cu and 0.023–0.430 wt% Ni (Tolstykh et al. 2008). The highest average PGE contents are observed in the taxitic leucogabbro (~3.4 ppm) and anorthosite (~2.2 ppm). One sample contained up to 4.1 ppm Pt and 7.8 ppm Pd; however, the average Pt/Pd ratios in the mineralized rocks range from 1 to 3. The concentrations of the other platinum group elements reach up to 18 ppb Os, 130 ppb Ir, 60 ppb Ru, and 80 ppb Rh (Tolstykh et al. 2008). The Au content in the sulfide-poor anorthosites does not exceed 250 ppb, on average.

Analytical techniques

Major element compositions of the samples were determined by X-ray fluorescence at the University of Tasmania using standard procedures. The concentrations of PGE, gold, and base metals in representative rock samples were determined at ACMELABS (Vancouver, British Columbia, Canada) and GEOLABS (Sudbury, Ontario, Canada): the concentrations of Cu, Cd, Ag, and Au were analyzed by ultra-trace inductively coupled plasma mass spectrometry (ICP-MS) method following an aqua regia digestion; the concentrations of PGE were determined by ICP-MS following fire assay fusion.

MLA analysis

Quantification of the proportions of sulfide minerals in poorly mineralized samples was performed on a FEI Quanta 600 scanning electron microscope (SEM) fitted with EDAX Sapphire SUTW Si(Li) energy-dispersive spectrometers at the Central Science Laboratory of the University of Tasmania in Hobart (Australia). Two automated methods of the Mineral Liberation Analyzer (MLA) software package were used. Both methods used similar beam conditions (20–25 kV accelerating voltage, around 3 nA beam current) and magnification (×150), collecting 60-ms energy-dispersive (ED) spectra.

The XMOD_STD method performs point counting based on collection of ED spectra on a grid with user-defined spacing. The spacing was adjusted in order to collect at least 10,000 spectra per sample. During acquisition, the collected spectra are compared to a set of reference spectra. If a spectrum cannot be matched, the beam position is shifted slightly and another spectrum is collected, assuming the original spectrum has been acquired on a grain boundary. This is repeated to a maximum of five spectra. If no match can be found after six attempts, the spectrum is defined as unknown mineral. XMOD_STD was run at 512 × 400 pixels frame resolution, corresponding to a pixel size of 3.52 × 3.52 μm or ~12 μm².

The SPL_Lt method is designed to target rare phases. It collects a spectrum for every grain above a user-defined size threshold, which also falls into a user-defined window of backscattered electron (BSE) intensity. This method is beneficial for samples with small overall amounts of sulfide minerals as it can be set up to ignore phases which are not of interest, in this case the common silicates. Compared to XMOD_STD, the SPL_Lt approach allows for collecting every grain above a certain size, not just the sulfide grains which happen to fall on the XMOD_STD point counting grid. The SPL_Lt method was run at 1024 × 800 pixels frame resolution, corresponding to a pixel size of 1.76 × 1.76 μm or ~3 μm². A threshold of 12 pixels was set for the grain size.

LA-ICP-MS analysis

The concentrations of Fe, Cu, Ni, Co, Zn, Ag, Re, Cd, PGE, and Au in sulfide minerals were determined by laser ablation ICP-MS (LA-ICP-MS) analysis at CODES, University of Tasmania. The method used follows that from Danyushevsky et al. (2011), Guillong et al. (2011), and Gilbert et al. (2013) and is described briefly here. Two laser ablation microprobes were employed: a UP213 solid-state Nd:YAG instrument from New Wave Research, equipped with a custom-made small-volume constant geometry ablation cell, and a RESOLUTION S-155 193-nm excimer laser from Resonetics. Both instruments were coupled to an Agilent 7700s quadrupole ICP-MS. Quantification was performed

following standard methods (Longerich et al. 1996) using an in-house software. Fe and Ni were used as the internal standards. PGE and Au were quantified using NiS-3 as the calibration standard (Gilbert et al. 2013) and all other elements using STDGL2b2 as the calibration standard (Danyushevsky et al. 2011). Interferences on Pd, Rh, and Ru were assessed by ablating pure Cu, Ni, Co, and Zn metals (Guillong et al. 2011), and all analyses were corrected accordingly. Isobaric interference of Cd^{106} on Pd^{106} was monitored by recording Cd^{110} intensities. Analyses were performed with a laser beam size of 22–40 μm and laser frequency of 5 Hz in an atmosphere of pure He. Each analysis consisted of 30 s gas background acquisition (laser off) followed by 60 s of signal acquisition. Ablated aerosol was transported to the ICP-MS in a mixture of He and Ar carrier gas.

Results

PGE-rich sulfide-poor mineralization

Our SEM study of three small fragments of anorthosite from the PGE Reef I revealed the presence of 22 PGM grains (~2–35 μm), including moncheite $(\text{Pt,Pd})(\text{Te,Bi})_2$ ($n = 6$), paolovite $(\text{Pd,Pt})_2(\text{Sn,Te})$ ($n = 5$), atokite $(\text{Pd,Au})(\text{Sn,As,Sb})$ ($n = 4$), and merenskyite $\text{Pd}(\text{Te,Bi})_2\text{-Pt}(\text{Te,Bi})_2$ ($n = 2$). Thus, both tellurides and bismutotellurides of Pt and Pd are most abundant in Reef I, with 50 % of the PGMs containing platinum (Kislov 1998, 2013). The SEM results revealed that almost all PGE/Au/Ag-bearing minerals occur in close spatial association with sulfides, usually along their boundaries or as aggregates with pentlandite and chalcopyrite (Fig. 5e).

These observations suggest the formation of the PGMs either at the late stages of crystallization of a PGE-rich sulfide melt or via subsolidus exsolution from sulfide minerals. The sulfide-related origin of PGMs is also supported by their presence as numerous inclusions (<5 μm size) in sulfide minerals. Additional evidence for the existence of an original PGE-rich sulfide liquid includes the high Pd content in pentlandite, ranging from 50 to 359 ppm, with an average of 235 ± 84 ppm ($n = 10$). Pentlandite also contains 6.9 ± 6.5 ppm Rh,

1.9 ± 2.0 ppm Ir, 0.93 ± 0.64 ppm Ru, 0.55 ± 0.30 ppm Os, 0.30 ± 0.12 ppm Re, 34.8 ± 12.1 ppm Ag, and 25.1 ± 15.5 ppm Te. However, the Pt and Au contents in pentlandite were commonly below the detection limits (20–40 ppb).

Sulfide-poor horizon in dunite

The horizon of poorly mineralized dunite (PMD) is marked by an ~5-fold increase in the S content from the background values 0.02–0.03 to 0.09–0.14 wt% (Fig. 6), reaching locally 0.6 wt% over a distance of several centimeters. These irregular variations in S contents are also reflected in the contents of Cu, Ni, and, particularly, IPGE (Fig. 6). The increase in S contents corresponds to a decrease in the abundance of intercumulus plagioclase and clinopyroxene and an increase in the amount of cumulus olivine in the uppermost plagiodunite.

Petrography of sulfides

Sulfides within the PMD horizon occur as small (0.1–0.3 mm) aggregates or larger (up to 1 mm) composite blebs, made up of pentlandite \pm chalcopyrite and/or pyrrhotite. The most common form is interstitial aggregates between olivine grains (Fig. 7). Close association of sulfides with phlogopite and spinel is widespread. In some cases, large sulfide inclusions were found in the intercumulus chromite (A and B in Fig. 8). Only occasional oxidation of sulfide is observed in these rocks.

Directly below the PMD horizon, there is an ~10-m-thick layer of sulfide-depleted (0.03–0.04 wt% S), chromite-enriched (~1 wt% Cr_2O_3) plagiodunite, which contains areas of fine round sulfides. This suggests that sulfide immiscibility possibly occurred in situ during the late stages of solidification of the mesocumulate poikilitic P1-dunite.

Dihedral angles and morphology of sulfides

Intercumulus sulfides in the lower part of the PMD horizon are characterized by low to moderate dihedral angles (mostly $\theta \leq 60^\circ$) and also form capillary-like textures between cumulus olivine (Fig. 7a, b). This suggests that the sulfide liquid wetted the surrounding olivine crystals, resulting

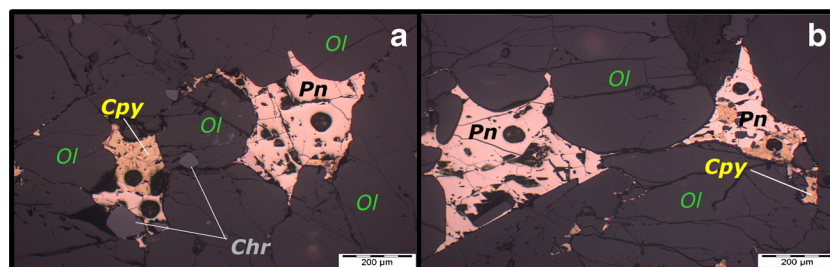
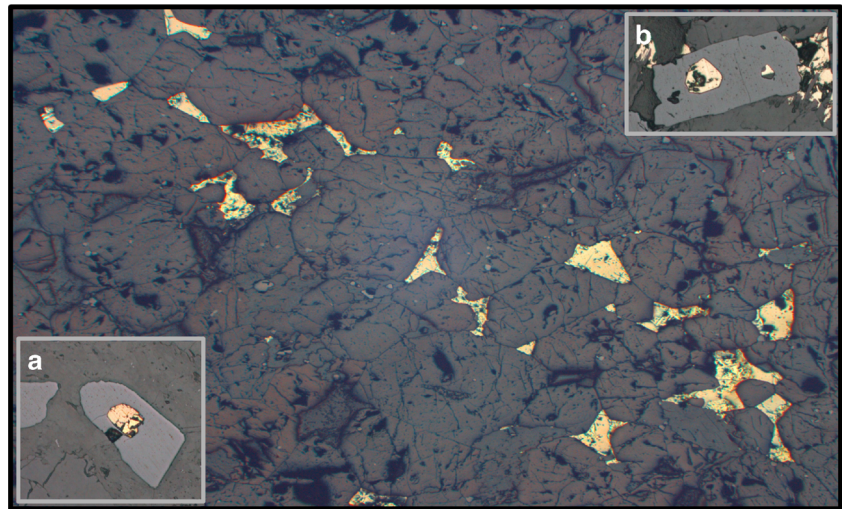


Fig. 7 Photomicrographs (reflected light) of interstitial sulfides, subhedral or euhedral cumulus olivine, and chromite from the lower poorly mineralized dunite. **a** 07DV124-4 ($h = 189$ m, 0.14–0.18 wt% S). **b** 07DV124-5 ($h = 228$ m, 0.10–0.28 wt% S). Black circles are pits after laser ablation

Fig. 8 Photomicrograph (reflected light) of the distribution of interstitial sulfides in dunite 07DV124-8. *Insets* represent sulfide inclusions in intercumulus chromite from the lowest dunite. *A* 07DV124-4, chromite crystal ~250 μm long hosted by phlogopite. *B* 07DV124-5, chromite crystal ~300 μm long between two olivine crystals and phlogopite (see *dark gray crystal to the left*)



locally in irregular-shaped areas of interconnected sulfides in three dimensions (Jung and Waff 1998; Barnes et al. 2008). It is commonly interpreted as a result of sulfide solidification in situ due to the inability of sulfide melt to migrate through the pore space of olivine cumulate.

However, toward the top of the PMD horizon, higher dihedral angles ($60^\circ \leq \theta \leq 115^\circ$; Fig. 8), including round sulfides in contact with interstitial plagioclase and phlogopite, suggest non-wetting behavior of the sulfide liquid, leading to the formation of separate droplets and allowing for coalescence to produce larger convex blebs (Barnes et al. 2008, 2011). This supports the hypothesis that under the effect of gravity, such a “non-wetting” sulfide liquid can infiltrate through the olivine cumulate pile from above (Chung and Mungall 2009), probably at the late stages of solidification of the cumulates (Ariskin et al. 2013a). Such a dual wetting behavior of the sulfide liquid in ultramafic cumulate piles has been described previously, suggesting that the Ni, Co, and Cu contents of the sulfide liquid can influence the wetting behavior (Rose and Brenan 2001).

Mineralogy of sulfides

Proportions between sulfide minerals determined using the MLA were used to calculate the average sulfide compositions for each sample. This required thorough pre-screening of the samples to find areas with maximum amounts of sulfide grains exposed on the polished surface. This is particularly important for samples with low whole-rock sulfur contents (<0.1 wt%).

The MLA analysis was performed on 25 samples (31 rock mounts in total), including 1 sample of picrodolerite DV30-1 (chilled rocks), 11 samples of plagiodunite, and 13 samples of the lower dunite. These data are

summarized in Table 2 and Fig. 9. Sulfides in plagiodunite and adcumulate dunite typically contain more than 60 vol% pentlandite and are relatively Po-poor. They range from almost pure pentlandite to 40 vol% Cpy+Cub (Fig. 9c). Sulfides in plagiodunite contain a higher proportion of pyrrhotite, reaching up to 40 vol% in some samples (Fig. 9c). In contrast, sulfides from the chilled picrodolerite are pyrrhotite-rich, containing only ~12 vol% of pentlandite.

Geochemistry of sulfides

Trace element concentrations in sulfide minerals were determined by LA-ICP-MS in 24 samples from the poorly mineralized horizon (Fig. 10). In total, 358 sulfide grains were analyzed (257 pentlandite grains from all samples, 63 pyrrhotite grains from 18 samples, 23 chalcopyrite grains from nine samples, and 13 cubanite grains from seven samples). Pyrrhotite was not analyzed from samples where its abundance is <1 vol%, whereas chalcopyrite could not be analyzed from samples with the proportion of Cu-rich minerals <5–10 vol% due to the absence of grains with sufficient size for LA-ICP-MS analysis. Similarly, sufficiently large cubanite grains were found only in seven samples that have relatively high proportions of Cu-rich sulfides (>15 %). Figure 10 presents the entire range of metal contents in pentlandite, pyrrhotite, chalcopyrite, and cubanite.

Similar to other PGE-mineralized intrusions (Great Dyke, Penikat, and Bushveld; Barnes et al. 2008), most PGEs (Os, Ir, Ru, Pd, and Rh) and Re are concentrated in pentlandite, where the concentrations are, on average, one order of magnitude higher than in the coexisting pyrrhotite. Ag and Cd in pentlandite and pyrrhotite display a large range of concentration (~0.2–100 ppm), whereas Au and Pt have low concentrations, commonly

Table 2 Proportions of base metal sulfides in the “average sulfide”

Sample	<i>h</i> (m)	S (wt%)	Rock	MLA	Po (%)	Pn (%)	Cpy (%)	Cub (%)	Cpy+Cub
DV30-1	0.4	0.07	Picrodolerite	<i>X</i>	76.21	12.90	7.66	3.23	10.89
				<i>S</i>	78.68	11.99	8.66	0.66	9.33
07DV 124-1b	150.0	0.04	Pl-dunite	<i>X</i>	25.00	68.75	0.00	6.25	6.25
07DV 124-1c	150.0	0.04	–	<i>S</i>	16.42	80.16	2.87	0.54	3.42
13DV547-10	156.0	0.03*	–	<i>S</i>	14.73	68.86	8.65	7.77	16.42
09DV 501-7	158.0	0.03	–	<i>X</i>	15.15	78.39	6.46	0.00	6.46
09DV 501-7c	158.0	0.03	–	<i>X</i>	8.33	83.33	0.00	8.33	8.33
07DV 124-3a	181.0	0.03	–	<i>X</i>	33.45	66.38	0.17	0.00	0.17
			–	<i>S</i>	20.48	75.82	3.49	0.22	3.70
07DV 124-3b	181.0	0.03	–	<i>X</i>	39.31	60.34	0.35	0.00	0.35
07DV 124-4ab	189.0	0.13	–	<i>X</i>	41.94	49.23	8.83	0.00	8.83
09DV 501-25	190.0	0.08	–	<i>X</i>	37.72	50.27	12.00	0.00	12.00
09DV 501-29	197.0	0.02	–	<i>X</i>	4.86	94.54	0.60	0.00	0.60
07DV124-4a	200.0	0.14	–	<i>X</i>	9.92	58.68	11.57	19.83	31.40
			–	<i>S</i>	16.17	60.55	17.28	6.00	23.28
09DV 501-40	216.0	0.07	–	<i>X</i>	0.54	80.94	18.52	0.00	18.52
			–	<i>S</i>	0.00	81.69	13.76	4.55	18.31
09DV 501-42	219.0	0.10	–	<i>X</i>	15.06	69.60	15.33	0.00	15.33
09DV 501-46	223.0	0.03	–	<i>X</i>	30.03	61.65	8.32	0.00	8.32
07DV124-5	228.0	0.28	Dunite	<i>X</i>	0.00	85.71	9.52	4.76	14.29
			–	<i>S</i>	1.09	89.88	3.95	5.09	9.03
09DV 501-52	229.0	0.03	–	<i>S</i>	0.23	95.24	4.37	0.17	4.54
09DV501-53	230.0	0.17	–	<i>X</i>	0.00	97.00	2.62	0.37	3.00
			–	<i>S</i>	0.00	95.59	3.89	0.52	4.41
09DV501-54	233.0	0.22	–	<i>X</i>	0.00	57.61	21.74	20.65	42.39
			–	<i>S</i>	0.07	58.29	32.56	9.09	41.64
07DV124-6	243.0	0.39	–	<i>X</i>	0.00	95.16	3.23	1.61	4.84
			–	<i>S</i>	0.13	77.88	13.84	8.14	21.99
09DV 501-61	252.0	0.18 ^a	–	<i>S</i>	0.01	79.56	13.99	6.44	20.43
09DV501-63	258.0	0.10	–	<i>S</i>	5.30	78.61	5.97	10.11	16.08
09DV 501-65	263.0	0.06	–	<i>X</i>	27.92	57.14	1.95	12.99	14.94
07DV 124-7	267.0	0.09	–	<i>S</i>	0.05	81.51	5.90	12.54	18.44
09DV 501-69	274.0	0.07 ^a	–	<i>S</i>	55.19	38.64	2.56	3.62	6.18
07DV124-8	286.0	0.58	–	<i>X</i>	41.18	58.82	0.00	0.00	0.00
			–	<i>S</i>	31.21	65.59	1.41	1.79	3.21
09DV 501-75	292.0	0.09	–	<i>S</i>	0.00	93.96	5.71	0.32	6.04
09DV 501-78	300.0	0.03 ^a	–	<i>S</i>	0.00	93.62	6.38	0.00	6.38

h is distance in meters from the lower contact

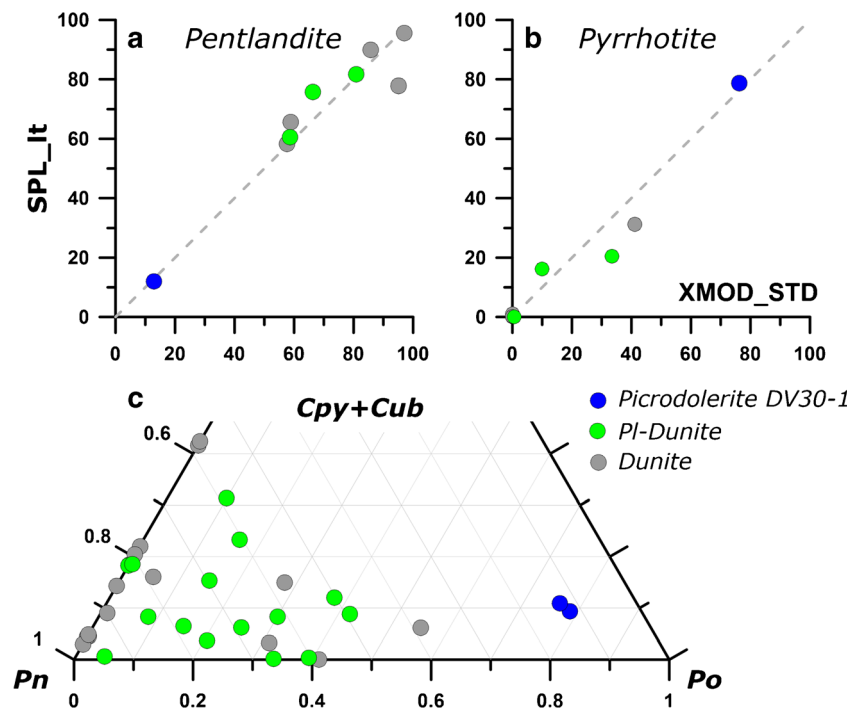
^a MLA methods: *X* is XMOD_STD and *S* is SPL_lt

<0.1 ppm. The concentrations of trace metals in chalcopyrite are similar to those in cubanite, with the Ag and Cd contents markedly higher than in pentlandite and pyrrhotite, whereas the Rh and Pd contents in chalcopyrite are intermediate between those in pentlandite and pyrrhotite.

The average sulfide compositions were calculated from the determined proportions of sulfide minerals and their average

trace element concentrations using a mass balance approach (Electronic supplementary materials (ESM) 1). Data for selected base metals (Fe, Ni, Cu, and Co), nine precious metals (Au, Ag, Pd, Pt, Rh, Ir, Os, Ru, and Re), and Cd are listed in Table 3, whereas their uncertainties and the original concentrations in sulfide minerals are given in ESM 2. There is an inverse correlation between the Fe and Ni contents, leading to

Fig. 9 Relative proportions of pentlandite, pyrrhotite, and Cu-rich phases in intercumulus sulfides from chilled picrodolerite, Pl-dunite, and lower dunite of the Yoko-Dovyren massif. **a, b** Comparison between XMOD_STD and SPL_Lt methods of the MLA analysis (nine samples). **c** Ternary diagram of sulfide mineral proportions



a wide range of Fe/Ni values (Fig. 11). This suggests that a Fe–Ni *mss* is the dominant sulfide phase present in both plagiodunite and adcumulate dunite. Os, Ru, and Rh display a strong positive correlation; however, samples from the lowermost Pl-dunite fall off the general trend toward lower Rh contents (Fig. 11). In contrast, Ir contents do not correlate with Ru.

Figure 12 presents variations of the average sulfide compositions as a function of their stratigraphic position.

There are no large variations in Cu contents, which range around 4–5 wt% in the sulfide, although a subtle trend of decreasing Cu contents is observed toward the top of the section. Two samples with anomalously high Cu contents include plagiodunite 07DV124-4 (32.4 vol% “Cpy+Cub” and ~8.5 wt% Cu) and adcumulate dunite 09DV501-54 (42.2 vol% “Cpy+Cub” and ~11.7 wt% Cu). Sulfides from these two samples are characterized by relatively high Au and low Os and Ru.

Fig. 10 Contents of precious metals and Cd in sulfides from the poorly mineralized plagiodunite to dunite horizon (Fig. 6). **a–d** Four sulfide minerals include average values (both normal and logarithmic), which are calculated when the number of analyses (n) is >3. Note that larger differences between the two average values are typical for elements which display a 3–4 order of magnitude range in concentrations

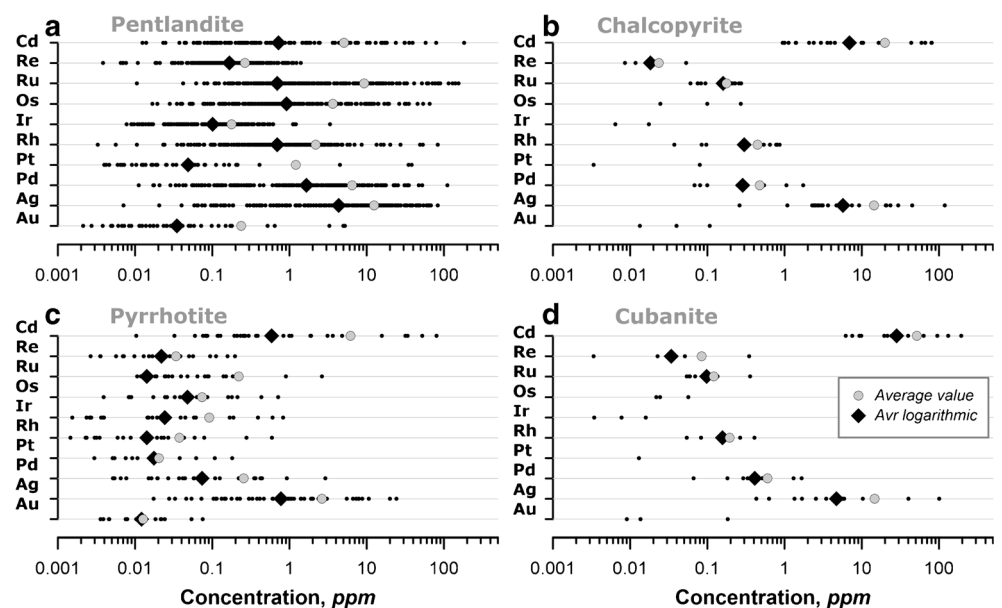


Table 3 Average compositions of sulfides in poorly mineralized plagioclone and dunite

Sample	Height (m)	Fe (wt%)	Ni (wt%)	Cu (wt%)	Co (wt%)	Ru99 (ppm)	Rh103 (ppm)	Pd106 (ppm)	Ag107 (ppm)	Cd111 (ppm)	Re185 (ppm)	Os189 (ppm)	Ir193 (ppm)	Pt195 (ppm)	Au197 (ppm)	S (wt%)
07DV124-1	150.0	41.21	20.46	1.41	0.89	14.96	1.78	1.20	16.33	0.82	0.03	5.96	0.107	0.089	0.014	36.04
13DV547-10	155.8	41.99	16.74	4.94	0.38	12.47	0.52	1.27	7.17	15.98	0.16	5.58	0.015	0.005	0.000	35.95
09DV501-7bc	158.0	40.90	20.11	2.46	0.54	26.87	0.30	2.03	7.30	11.26	0.08	11.16	0.052	0.000	0.010	36.00
09DV501-7	158.0	41.10	20.10	2.13	0.51	43.39	1.08	3.74	8.66	0.94	0.24	22.53	0.172	0.137	0.068	36.16
09DV124-3	181.0	46.05	16.99	0.18	0.59	0.17	0.05	5.04	6.21	6.39	0.06	0.20	0.061	0.119	0.036	36.19
09DV124-4AB	189.0	45.91	14.15	3.09	0.46	0.36	0.36	12.76	16.55	6.89	0.23	0.40	0.075	0.023	0.026	36.39
09DV501-25	189.8	45.45	14.55	3.59	0.43	11.42	3.98	4.69	4.71	7.03	0.10	4.62	0.139	0.043	0.022	35.99
09DV501-29	196.8	32.79	29.75	0.27	1.44	6.19	2.18	1.91	3.67	0.69	0.11	3.74	0.115	0.014	0.065	35.74
07DV124-4a	200.0	38.56	18.41	8.50	0.50	1.47	1.15	16.84	11.65	4.29	0.12	0.81	0.214	0.188	0.012	34.03
09DV501-40	216.2	34.70	26.17	2.55	0.42	1.67	1.22	0.40	6.42	1.55	0.47	0.58	0.090	0.024	0.016	36.15
09DV501-42	219.0	39.03	19.20	5.15	0.50	3.18	0.72	5.98	22.06	14.62	0.21	0.93	0.064	0.055	0.038	36.11
09DV501-46	223.0	42.45	18.05	2.85	0.43	0.56	0.22	6.46	26.37	18.81	0.05	0.29	0.057	0.031	0.005	36.22
07DV124-5	228.0	35.27	26.66	4.20	0.49	4.89	1.09	8.73	21.42	9.10	0.50	0.93	0.033	0.008	0.007	33.38
09DV501-52	229.0	28.82	32.40	1.66	0.76	1.73	0.13	0.04	4.04	1.55	0.09	0.36	0.118	0.002	0.008	36.36
09DV501-53	230.0	29.62	32.31	1.46	0.36	0.70	0.86	0.00	10.31	7.56	0.39	0.69	0.191	0.000	0.007	36.25
09DV501-54	232.8	34.83	17.83	11.71	0.26	0.41	0.35	0.79	6.98	6.92	0.39	0.18	0.073	0.061	0.117	35.37
07DV124-6a	243.0	32.35	32.31	1.59	0.40	1.08	0.54	0.16	3.20	2.41	0.44	0.34	0.180	0.000	0.003	33.34
09DV501-61	252.4	31.99	25.63	6.30	0.35	0.83	0.47	0.28	10.43	2.09	0.23	0.33	0.077	0.009	0.022	35.73
09DV501-63	258.0	37.42	21.73	4.44	0.46	2.19	0.66	8.20	19.38	1.20	0.22	0.78	0.131	0.003	0.016	35.94
09DV501-65	263.6	46.68	13.06	3.85	0.35	0.34	0.29	1.07	3.12	5.59	0.04	0.10	0.041	0.004	0.007	36.07
07DV124-7	267.0	35.07	23.32	5.38	0.45	1.26	0.70	2.08	12.06	11.87	0.09	0.56	0.185	0.010	0.005	35.78
09DV501-69	274.8	51.09	10.70	1.67	0.36	8.08	2.20	1.75	7.25	2.28	0.09	2.55	0.045	0.006	0.017	36.19
07DV124-8	286.0	51.06	15.23	1.95	0.43	0.58	0.38	1.60	21.42	18.44	0.04	0.13	0.050	0.000	0.002	31.33
09DV501-75	291.6	32.71	27.67	3.14	0.64	2.69	1.7092	0.14	12.05	5.994	0.12	0.66	0.40	0.000	0.016	35.77
09DV501-78	300.0	28.07	32.53	2.46	1.16	7.06	2.40	0.09	4.55	3.05	0.18	1.27	0.534	0.000	0.013	35.77

The listed compositions were calculated by Eq. 2 from Online Resource 1. For uncertainty of these calculations, see sheet “AVERAGE Sulfide comps” in Online Resource 2

Within plagioclone from the main part of the PMD horizon (Fig. 12), the highest concentrations of Os, Ru, and Rh in sulfides are observed within an ~7-m-thick layer at the base of the plagioclone, whereas Pd and Pt display maximum concentrations 3–4 m higher. The

maximum Re concentration is observed at a stratigraphic elevation of ~215–220 m, whereas Ag and Cd display a maximum at the top of the plagioclone. Au concentrations display a clear maximum at the base of the dunite zone.

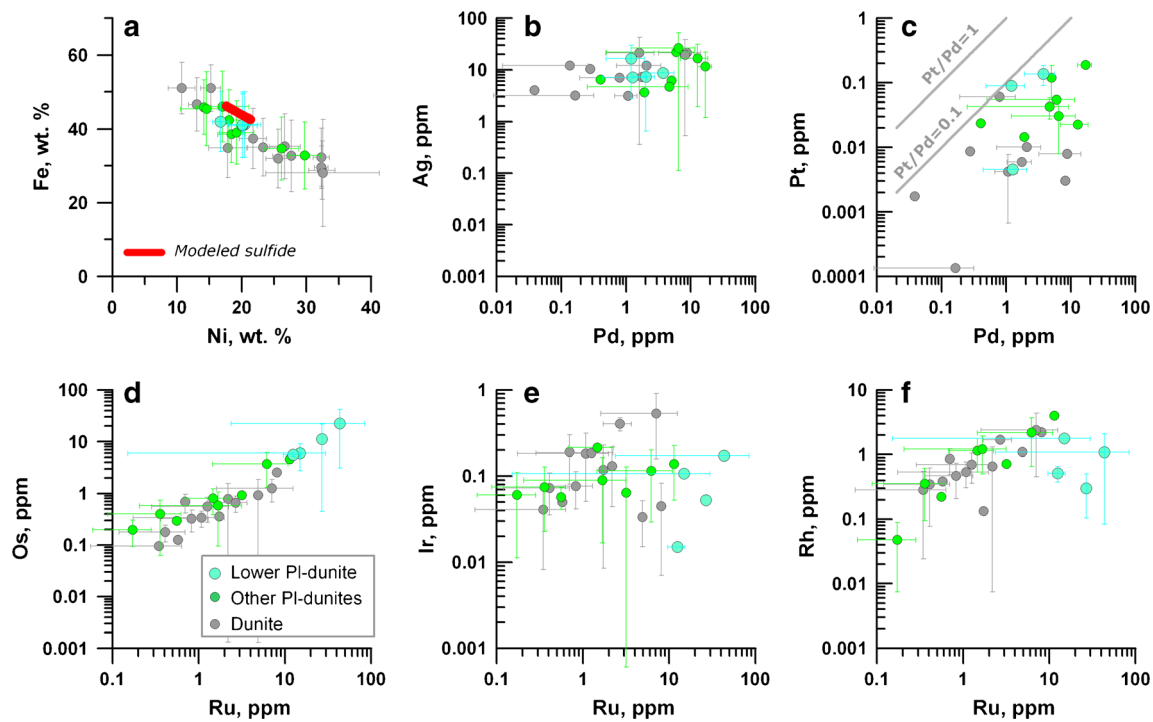


Fig. 11 a–f Fe vs. Ni and precious metal covariations in bulk sulfides from poorly mineralized PI-dunite to dunite horizon (Fig. 6). Concentrations are from Table 3. *Modeled sulfide* in (a) displays the compositional range of immiscible sulfide liquid simulated during

solidification of a multiply-saturated olivine-rich cumulate pile, which is compositionally identical to picrodolerite DV30-2 (Fig. 13). *Error bars* are shown according to Online Resource 2

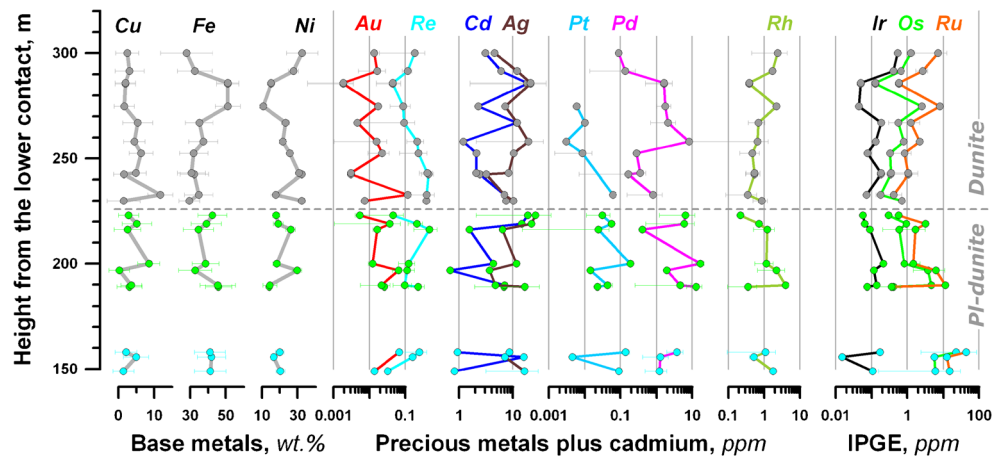
The distribution of these elements within dunite is more regular. Re, Au, and Pt display a general trend of depletion up to a stratigraphic height of ~275 m; Cd, Ag, and Pd form a thick zone of higher concentrations in the middle of the sequence, whereas Rh and IPGE tend to increase at the top of the sequence (Fig. 12).

Discussion

This study puts forward a hypothesis that the poorly mineralized dunite may provide insights into the earliest stages of the

formation, evolution, and migration of immiscible sulfide liquid in solidifying olivine-rich cumulate piles. One important conclusion from the MLA studies is that the observed differences in the amounts of base metal sulfides in the average sulfide from the PMD horizon (ranging from almost pure pentlandite to those containing ~40 % Cpy+Cub; Table 2) could result from sulfide fractionation in the olivine cumulate pile. As an alternative, an efficient Fe–Ni diffusive exchange between original immiscible sulfide liquid and the surrounding cumulus olivine may be suggested (Fig. 9; see Barnes et al. 2013). We believe that both processes could take place, with the sulfide fractionation recorded in rare sulfide

Fig. 12 Average sulfide compositions vs. stratigraphic position in the poorly mineralized horizon of the Yoko-Dovyren massif. Calculated sulfide compositions are from Table 3. *Colored circles* are the same as in Fig. 10. *Error bars* are shown according to Online Resource 2



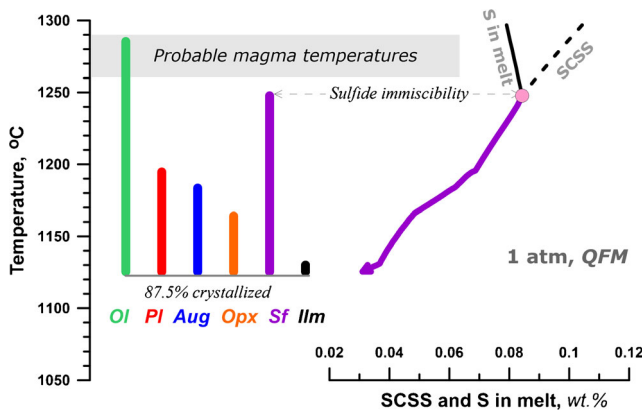


Fig. 13 Mineral crystallization sequence vs. evolution of sulfur concentration at sulfide solubility (SCSS) and S content in the melt during closed-system solidification of the parental magma modeled from the composition of Ol-rich picrodolerite DV30-2. Calculations were performed at 1 atm anhydrous conditions using COMAGMAT-5 (Ariskin et al. 2013b). Probable range of magma temperatures is consistent with previous estimates (Ariskin et al. 2009b, c)

assemblages containing >30 vol% pyrrhotite (Fig. 9). This is distinctly different from the average sulfide observed in the chilled picrodolerite DV30-1, which contains as much as 80 vol% Po at Pn/(Cpy+Cub) ratio around 1. Modern methods of thermodynamic modeling of sulfide-saturated magmatic systems (Ariskin and Danyushevsky 2014) give rise to estimates of the original sulfide liquid composition in each particular PMD rock.

COMAGMAT-5 (Ariskin et al. 2013b) allows for modeling cotectic crystallization of Fe–Ni sulfide liquid and silicate±oxide minerals from mafic melts at 1 atm under anhydrous conditions. Such conditions are appropriate for modeling the crystallization of the YDM parental magmas, as previous studies have demonstrated that the YDM has likely formed within the upper crust at low pressures (0.5–1 kbar) and that the parental magmas contained <0.5 wt% H₂O (Ariskin et al. 2009a).

We have modeled closed-system (i.e., equilibrium) crystallization of a chilled picrodolerite DV30-2 sampled ~1.4 m above the lower contact of the YDM (Online Resource 2). Its composition is similar to plagioperidotite

from the basal unit of the YDM (Fig. 3). It contains 0.05 wt% S, 24.4 wt% MgO, and ~0.14 wt% Ni. At ~1290 °C, which represents the estimated temperature of emplacement of the high-Fo type of the YDM parental magmas (Ariskin et al. 2009c), this composition contains ~37 wt% olivine Fo88 and silicate melt (Fig. 13). Sulfide immiscibility occurs at *T* ~ 1248 °C, i.e., 30–40 °C below the emplacement temperature, corresponding to ~40.4 wt% crystallization of olivine which, at that stage, has composition ~Fo87. The modeled crystallization sequence involves Ol → Ol+Sulf → Ol+Sulf+Pl → Ol+Sulf+Pl+Aug → Ol+Sulf+Pl+Aug+Opx → Ol+Sulf+Pl+Aug+Opx+Ilm (Fig. 13). This is consistent with the observed mineralogy of the S-bearing plagioperidotite (see description above), suggesting that these rocks crystallized as a closed system. The maximum modeled extent of crystallization was 87.5 wt% at ~1125 °C.

The contents of Ni and Fe in the modeled sulfide plot within the field of bulk sulfide compositions in plagiodunite and accumulate dunite (Fig. 11). As described above, these compositions are significantly richer in Ni compared to the sulfides present in the primitive picrodolerite DV30-1 sampled 0.4 m above the lower contact (Fig. 9). The reason for these differences is the variable amount of olivine in the parental magmas (higher in DV30-2; Fig. 3). The higher amount of olivine serves as a buffer of Ni contents in the silicate melt during closed-system crystallization, leading to the higher content of Ni in the equilibrium sulfide melt.

The results of COMAGMAT-5 modeling described above can be used to assess the concentrations of Cu and precious metals in the coexisting silicate and sulfide melt during crystallization, if their contents in the parental magmas and their sulfide/silicate melt partition coefficients are known.

Calculations of PGE contents in sulfides

Following from Ariskin and Danyushevsky (2014), in the case of equilibrium crystallization of a heterogeneous multiply-

Table 4 Contents of Cu, Cd, and four precious metals in sample DV30-2

Modeled elements	Cu (ppm)	Cd (ppb)	Ag (ppb)	Pd (ppb)	Pt (ppb)	Au (ppb)		
DV30-2, whole-rock composition	47.8	20	19	12.8	7.3	1.3		
Distribution coefficients	Sulfide droplet/MORB glass			Experimental values				
$D_i^{S/Melt}$	av	100	1005	67,000	min	125,000	4100	4100
	pref	107	1138	536,000	max	1,560,000	11,200	11,200

av and *pref* are the average and preferred values, respectively, for Cu, Cd, and Ag from Patten et al. (2013), whereas *min* and *max* characterize the range of experimental data for $D_i^{S/Melt}$ for Pd, Pt, and Au from Mungall and Brenan (2014)

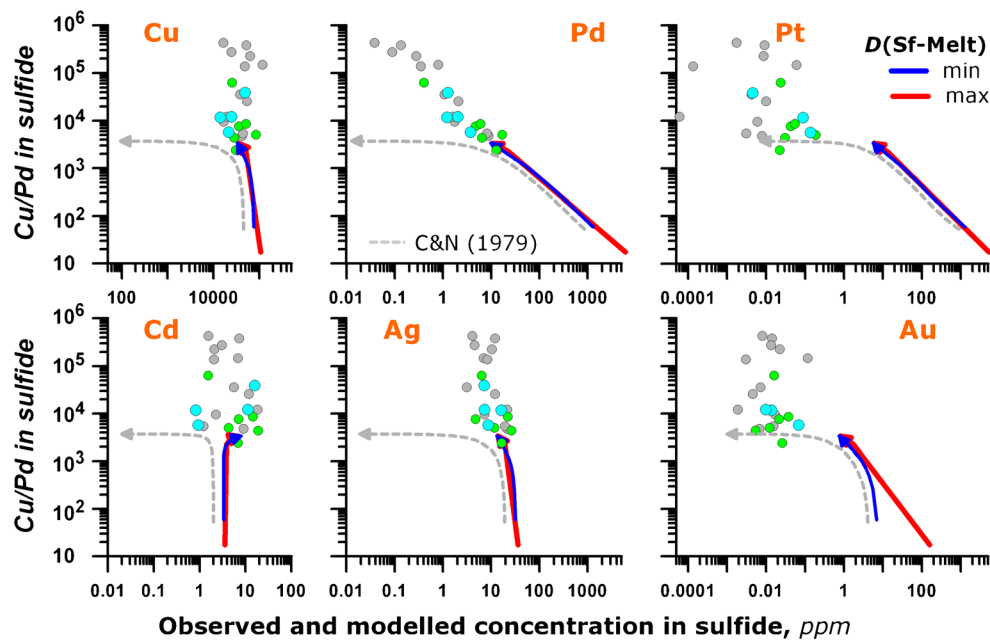


Fig. 14 Average compositions of sulfides from the poorly mineralized zone of the Yoko-Dovyren massif and modeled compositions of immiscible sulfide melt within the olivine cumulate pile. The calculations represent the closed-system crystallization of picrodolerite DV30-2 (Table 4), with modeled onset of sulfide immiscibility at 30–40 °C below the initial magma temperature (Fig. 13). The *min* and *max*

trajectories refer to the minimum and maximum values of $D_i^{Sf/Melt}$ listed in Table 4. *C&N* corresponds to the canonic *R*-factor equation, assuming a simple binary system sulfide+sulfate melt (Campbell and Naldrett 1979). Note that only calculations for the minimum $D_i^{Sf/Melt}$ values are shown for the *C&N* approach. *Colored symbols* as in Fig. 11

saturated system, the content of element *i* in the evolving melt may be calculated as

$$X_i^{Melt} = X_i^{Magma} \frac{(R + 1)}{(R + D_i^{Sf/Melt})(1 - F_{Min})} \quad (1)$$

where X_i^{Magma} is the content of element *i* in the parental magma (assuming closed-system crystallization), $D_i^{Sf/Melt}$ is its partition coefficient between sulfide and silicate melts, *R* is calculated as the silicate melt/sulfide ratio (f_{Melt}/f_{Sf} , i.e., *R*-factor after Campbell and Naldrett 1979), and F_{Min} is the sum of the fractions of other crystallizing phases (silicate minerals ± oxides), so that $F_{Min} = 1 - f_{Melt} - f_{Sf}$. Note that in Eq. 1, it is assumed that element *i* is perfectly incompatible in silicate/oxide minerals. When this is not the case, or when other phases may be present during crystallization (e.g., PGM), this equation would overestimate the concentrations of elements in the silicate and sulfide melts. Using the notations from Campbell and Naldrett (1979), the composition of the coexisting sulfide liquid is

$$Y_i^{Sf} = X_i^{Melt} D_i^{Sf/Melt} \quad (2)$$

Equation 1 takes into account the multiphase character of the crystallizing mineral assemblage, which leads to a slower depletion of the silicate and sulfide melts in chalcophile elements

compared to models assuming sulfide–silicate melt binaries. This is because continuous crystallization of silicate and oxide minerals enriches the silicate melt in these elements, as long as they remain incompatible in these minerals, whereas the proportion of sulfide melt remains low, commonly <1–1.5 wt% (Barnes 2007; Li and Ripley 2009; Ariskin et al. 2009b).

The contents of Cu, Cd, Ag, Au, Pt, and Pd in sample DV30-2 were assumed to be representative of their contents in the parental magma (Table 4). To calculate partitioning of these elements between the immiscible Fe–Ni sulfide melt and coexisting silicate melt, two sets of sulfide–silicate partition coefficients were used. The first set is based on LA-ICP-MS analyses of Cu, Cd, and Ag in sulfide droplets and their host fresh MORB glasses (Table 4; Patten et al. 2013). The second set includes experimental $D_i^{Sf/Melt}$ values for Pd, Pt, and Au, obtained at 1 atm, 1200 °C, and controlled f_{S_2} for a synthetic FeS + basalt analogue system (Table 4; Mungall and Brenan 2014).

The calculated compositions of sulfide melts at 87.5 wt% total crystallization match very closely the compositions of the bulk sulfide with the highest contents of Cu, Cd, Ag, and Pd (the lowest Cu/Pd values). Our interpretation of the natural sulfides with higher Cu/Pd values is that they may represent sulfide liquids that existed near silicate solidus. However, our modeling predicts much higher Au and Pt contents than what are observed in the samples (Fig. 14). The most likely

explanation is that Au and Pt dominantly reside in separate non-sulfide phases such as PGM and electrum; thus, their observed concentrations in the bulk sulfide are lower than in the modeled sulfide melt.

Factors affecting the distribution of IPGE in sulfides

Although Os and Ru display a strong positive correlation in all samples (Fig. 11), Ir and Rh are markedly lower in the bulk sulfide from the base of the plagiodunite (Fig. 11). These observations may indicate the existence of additional phase(s) that contain Ir and Rh, such as native alloys (Barnes and Fiorentini 2008) and/or chromite (Locmelis et al. 2011; Barnes et al. 2016).

To evaluate this possibility, we performed a preliminary LA-ICP-MS screening of 46 grains of chromite in two samples from the lowermost plagiodunite. In one of the samples (09DV501-7, 34 analyses of chromite) six relatively large (5–15 μm) Os+Ir±Ru inclusions were found. These results support recent observations by Locmelis et al. (2011) and Page and Barnes (2013) that chromite may act as an important phase controlling the whole-rock budget of Os, Ir, Ru, and Rh, in addition to PGM and sulfides. Interestingly, rare disseminated sulfides from sample 09DV501-7 (which contains only 0.03 wt% S) have the highest average concentrations of Ru (43.4 ± 41.0 ppm) and Os (22.5 ± 19.4 ppm; Fig. 11). Thus, one cannot exclude a possibility of diffusive exchange of IPGE between chromite and sulfide, as has been suggested by Barnes et al. (2016).

Another unusual feature of samples from the lowest plagiodunite is that their bulk rock compositions are characterized by the highest Pt/Pd ratio (1.56 ± 0.78), which is approximately four times higher than the average Pt/Pd in the overlying rocks (0.39 ± 0.36). The low Pt/Pd values of the bulk sulfide from these samples (<0.1 ; Fig. 11) argue for the presence of a separate Pt-bearing mineral phase.

Evidence for sulfide migration at the latest stages of solidification of the cumulate piles

The average Ni content of the bulk sulfides through the mineralized dunite horizon (21.7 ± 6.5 wt% Ni, $n = 24$) matches closely the calculated composition of the sulfide liquid (Fig. 11). Very similar compositions (19.4 ± 1.7 wt% Ni) are found in sulfides from the lowermost S-depleted plagiodunite (<0.04 wt% S; Figs. 6 and 11). A possible explanation is that all rocks from this ~8-m-thick horizon crystallized as a closed system, preserving the entire mass of the immiscible sulfide liquid. This conclusion is supported by the numerous finely dispersed sulfides, both in the poikilitic plagioclase matrix and (in rare cases) as separate inclusions in olivine. The highest Os and Ru contents in these sulfides may be considered as additional evidence for their primary nature (Figs. 11 and 12 and Table 3).

A possible explanation for the wide range of Fe/Ni values in the bulk sulfide from the plagiodunite and adcumulate dunite (Figs. 9 and 11) is that they reflect percolation of the *ms* sulfide liquid at the late stages of solidification of the olivine cumulate piles. This is in agreement with the high diversity of dihedral angles of sulfides, ranging from $\theta \geq 90^\circ$ (“no-wetting” behavior; Fig. 8) to $\theta \leq 60^\circ$, indicative of sulfide wetting olivine grains, leading to entrapment of sulfides in the pore space of the olivine cumulates (Fig. 7).

The possibility of sulfide percolation through the poorly mineralized zone is indirectly supported by the distribution of precious metals in the average sulfide. The high range of their contents, which spans 3–4 orders of concentration (Fig. 10), is difficult to reconcile with in situ sulfide crystallization from the same intercumulus melt in compositionally similar cumulates.

Sulfides in plagiodunite are characterized by maxima in PGE concentrations, which occur at variable distances from the contact (Fig. 12). Os, Ru, and Rh display a maximum at the bottom of the horizon, Pt and Pd display a maximum several meters higher, whereas Ag, Cd, and Re display a maximum toward the top of the horizon. As this sequence is consistent with decreasing values of the sulfide–silicate melt partition coefficients for these metals (Patten et al. 2013; Mungall and Brenan 2014), it may indicate that it reflects differential fractionation of sulfides, as has been discussed by Naldrett and Wilson (1990) for the Great Dike and by Barnes (1993) for the Munni Munni intrusion.

Concluding remarks

The Yoko-Dovyren layered massif contains a range of sulfide mineralization types, from widespread disseminated sulfides (Fig. 2) to massive and net-textured Cu–Ni sulfides at the base of the massif, to PGE-rich anorthosite within the mafic part of the intrusion. This study focused on the texture, mineralogy, and geochemistry of the poorly mineralized plagiodunite and the lowermost dunite, which record information on the onset of sulfide saturation within the cumulate pile. To better constrain this process, we combined estimates of the bulk sulfide compositions in each rock type with numerical modeling of immiscible sulfide melt compositions using COMAGMAT-5 (Ariskin et al. 2013b; Ariskin and Danyushevsky 2014). Such a combination is an effective petrological tool for understanding the early stages of sulfide saturation in large layered intrusions.

An important aspect of our approach is the use of MLA to characterize the bulk sulfide composition of poorly mineralized rocks, which contain <0.1 wt% S. For this approach, it is essential to carefully pre-screen samples to choose areas with the most abundant sulfides. This allows for an estimate of the proportions of the sulfide minerals (Pn, Po, Cpy, and Cub) with an uncertainty of ~5%, which is acceptable for further

calculations of the average weighted sulfide composition using geochemical data from the LA-ICP-MS of individual sulfide minerals.

Results of numerical modeling of sulfide compositions in initially sulfur-undersaturated olivine cumulates demonstrate a strong effect of the decreasing fraction of the silicate melt, due to crystallization of silicate and oxide minerals, on the composition of the immiscible intercumulus sulfide liquid.

Acknowledgments We acknowledge support of AngloAmerican, BHP Billiton, Votorantim Metais, and the Australian Research Council through funding to CODES (Hobart, Australia) at the initial stages of the projects (AMIRA project P962, 2007–2010). The authors also thank the University of Tasmania for providing Visiting Scholarships to AAA at the UTAS in 2011 and 2014 and the Russian Foundation for Basic Research for their support during 2008–2014 (projects 08-05-00194a, 11-05-00268a, and 14-05-00216a). ML Fiorentini also acknowledges support from the Australian Research Council through the Future Fellowship Scheme (FT110100241) and Foundation Project 2a of the Centre of Excellence for Core to Crust Fluid Systems. This is contribution 639 from the ARC Centre of Excellence for Core to Crust Fluid Systems (<http://www.cafs.mq.edu.au>). We also wish to thank Masha Anosova and Kostya Ryazantsev (Vernadsky Institute, Moscow) for their assistance with sample preparation, Paul Olin with help with LA-ICP-MS analyses at the University of Tasmania, and Veniamin Polyakov (Institute of Experimental Mineralogy, Russia) for his help with statistical calculations. Thorough comments of Evgeny Koptev-Dvornikov (Moscow State University, Moscow) on the textures of ultramafic cumulates were invaluable. We gratefully acknowledge Dr. Elinor Morrisby for her editing of the earlier version of the manuscript. Wolf Maier, Reid Keays, and Georges Beaudoin are thanked for their careful reviews. The authors would like to acknowledge the contributions of the late Eduard Konnikov who worked on this project during 2007–2011.

References

- Ariskin AA, Danyushevsky LV (2014) The sulfide COMAGMAT: modeling R-factor and Cu-Ni-PGE tenors in sulfides for multiple-saturated magmas. *Proceedings of the 12th International Platinum Symposium, Yekaterinburg, Russia*, 1:15–16
- Ariskin AA, Konnikov EG, Danyushevsky LV, Kislov EV, Nikolaev GS, Orsoev DA, Barmina GS, Bychkov KA (2009a) The Dovyren Intrusive Complex: problems of petrology and Ni sulfide mineralization. *Geochem Intern* 47:425–453
- Ariskin AA, Barmina GS, Bychkov KA, Danyushevsky LV (2009b) Parental magmas of mafic layered intrusions: using an updated COMAGMAT model for calculations of sulfide-silicate cotectics during their crystallization. *Northwest Geol* 42:1–3
- Ariskin AA, Danyushevsky LV, Konnikov EG, Barmina GS, Nikolaev GS (2009c) Use of olivine control lines and the COMAGMAT model for evaluation of the parental magma composition of the Yoko-Dovyren layered intrusion. *Proceedings of the 3rd International Conference ‘Mafic-Ultramafic Complexes of Folded Regions and Related Deposits’, Yekaterinburg-Kachkanar, Russia*, 1:57–60
- Ariskin AA, Danyushevsky LV, McNeill AW, Nikolaev GS, Kostitsyn YA (2013a) The Yoko-Dovyren layered massif (southern Siberia, Russia): fingerprints of an open magma chamber and compaction of original cumulates conjugated with sulphide percolation process. *Proceedings of the 12th SGA Biennial Meeting, Uppsala, Sweden*, 3:941–943
- Ariskin AA, Danyushevsky LV, Bychkov KA, McNeill AW, Barmina GS, Nikolaev GS (2013b) Modeling solubility of Fe-Ni sulfides in basaltic magmas: the effect of Ni in the melt. *Econ Geol* 108:1983–2003
- Ariskin AA, Kostitsyn YA, Konnikov EG, Danyushevsky LV, Meffre S, Nikolaev GS, McNeill A, Kislov EV, Orsoev DA (2013c) Geochronology of the Dovyren Intrusive Complex, northwestern Baikal area, Russia, in the Neoproterozoic. *Geochem Intern* 51: 859–875
- Ariskin AA, Danyushevsky LV, Konnikov EG, Maas R, Kostitsyn YA, McNeill AW, Meffre S, Nikolaev GS, Kislov EV (2015) The Dovyren Intrusive Complex (northern Baikal region, Russia): isotope-geochemical markers of contamination of parental magmas and extreme enrichment of the source. *Russian Geol Geophys* 56: 411–434
- Barnes SJ (1993) Partitioning of the platinum group elements and gold between silicate and sulphide magmas in the Munni Munni Complex, Western Australia. *Geochim Cosmochim Acta* 57:1277–1290
- Barnes SJ (2007) Cotectic precipitation of olivine and sulfide liquid from komatiite magma and the origin of komatiite-hosted disseminated nickel sulfide mineralization at Mount Keith and Yakabindie, Western Australia. *Econ Geol* 106:298–304
- Barnes SJ, Fiorentini ML (2008) Iridium, ruthenium and rhodium in komatiites: evidence for alloy saturation. *Chem Geol* 257:44–58
- Barnes SJ, Fiorentini ML, Austin P, Gessner K, Hough RM, Squelch AP (2008) Three-dimensional morphology of magmatic sulfides sheds light on ore formation and sulfide melt migration. *Geology* 36:655–658
- Barnes SJ, Osborne GA, Cook D, Barnes L, Maier WD, Godel B (2011) The Santa Rita nickel sulfide deposit in the Fazenda Mirabela intrusion, Bahia, Brazil: geology, sulfide geochemistry, and genesis. *Econ Geol* 106:1083–1110
- Barnes SJ, Godel B, Güreş D, Brennan JM, Robertson J, Paterson D (2013) Sulfide-olivine Fe-Ni exchange and the origin of anomalously Ni rich magmatic sulfides. *Econ Geol* 108:1971–1982
- Barnes S-J, Page P, Prichard HM, Zientek ML, Fisher PC (2016) Chalcophile and platinum group element distribution in the ultramafic series of the Stillwater Complex, Mt. USA—implications for processes enriching chromite layers in Os, Ir, Ru, and Rh. *Mineral Depos* 51:25–47
- Campbell IH, Naldrett AJ (1979) The influence of silicate:sulfide ratios on the geochemistry of magmatic sulfides. *Econ Geol* 74:1503–1506
- Chung HY, Mungall JE (2009) Physical constraints on the migration of immiscible fluids through partially molten silicates, with special reference to magmatic sulfide ores. *Earth Planetary Sci Lett* 286: 14–22
- Danyushevsky LV, Robinson P, Gilbert S, Norman M, Large R, McGoldrick P, Shelley JMG (2011) Routine quantitative multi-element analysis of sulphide minerals by laser ablation ICP-MS: standard development and consideration of matrix effects. *Geochemistry: Exploration, Environment, Analysis* 11:51–60
- Denisova MV (1961) Copper-nickel sulfide mineralization in a mafic-ultramafic massif of the Baikal Folded area. In: *Proceedings on Geology and Mineralogy of Ore Deposits of USSR (new series 60)*. VSEGEI, Leningrad, pp 37–46 (in Russian)
- Distler VV, Stepin AG (1993) Low-sulfide PGE-bearing unit of the Yoko-Dovyren layered ultrabasic-basic intrusion, Northern Transbaikalia. *Dokl Akad Nauk* 328:498–501 (in Russian)
- Ernst RE, Hamilton MA, Soderlund U (2012) A proposed 725 Ma Dovyren-Kingash LIP of southern Siberia, and possible reconstruction link with the 725–715 Ma Franklin LIP of northern Laurentia. *Abs vol. 35, GAC-MAC Joint Annual Meeting “Geoscience at the Edge”, May 27–29, St. John’s, Newfoundland and Labrador, Canada*
- Gilbert S, Danyushevsky L, Robinson P, Wohlgemuth-Ueberwasser C, Pearson N, Savard D, Norman M, Hanley J (2013) A comparative study of five reference materials and the Lombard meteorite for the

- determination of the platinum-group elements and gold by LA-ICP-MS. *Geostand Geoanal Res* 37:51–64
- Grudin MI (1963) Geology and petrology of the Dovyren gabbro-peridotite massif northern Baikal area. *Geol Geophys* 4:78–91 (in Russian)
- Guillong M, Danyushevsky L, Waelle M, Raveggi M (2011) The effect of quadrupole ICPMS interface and ion lens design on argide formation. Implications for LA-ICPMS analysis of PGE's in geological samples. *J Anal Atom Spec* 26:1401
- Gurulev SA (1965) Geology and genesis of the Yoko-Dovyren gabbro-peridotite massif. Nauka, Moscow (in Russian)
- Gurulev SA (1983) Genesis of layered mafic intrusions. Nauka, Moscow (in Russian)
- Heaman LM, LeCheminant AN, Rainbird RH (1992) Nature and timing of Franklin igneous event, Canada: implications for a Late Proterozoic mantle plume and the break-up of Laurentia. *Earth Planet Sci Lett* 109:117–131
- Jowitt SM, Ernst RE (2013) Geochemical assessment of the metallogenic potential of Proterozoic LIPs of Canada. *Lithos* 174:291–307
- Jung H, Waff HS (1998) Olivine crystallographic control and anisotropic melt distribution in ultramafic partial melts. *Geophys Res Lett* 25:2901–2904
- Keays R, Lightfoot P, Hamlyn P (2011) Sulfide saturation history of the Stillwater Complex, Montana: chemostratigraphic variation in platinum group elements. *Mineral Depos* 47:151–173
- Kislov EV (1998) The Yoko-Dovyren layered massif. BNTsRAN, Ulan-Ude (in Russian)
- Kislov EV (2010) The nickel reserve of Russia: the northern Baikal nickel-fertile province. *Globus (Geology and Business)* 13:30–37 (in Russian)
- Kislov EV (2013) Ni–Cu deposits of the northern Baikal region. IAGR Conference Series 14. Abs vol. IAGR Ann Conv, 10th International Symposium on “Gondwana to Asia”, Institute of Geoscience and Mineral Resources, Daejeon, pp 58–60
- Kislov EV, Konnikov EG, Orsoev DA, Pushkarev EV, Voronina LK (1995) Constraints on the genesis of low-sulphide PGE mineralization at the Ioko-Dovyren layered massif, northern Transbaikalia, Russia. In: Pasava J, B Kribek B, Zak K (eds) *Mineral deposits: from their origin to their environmental impacts*. AA Balkema, Rotterdam, pp 121–124
- Konnikov EG (1986) The Precambrian differentiated ultramafic-mafic complexes of the Transbaikalia region. Nauka, Novosibirsk (in Russian)
- Konnikov EG, Kislov EV, Kacharovskaya LN (1988) New data about petrology and ore content of the Ioko-Dovyren nickel-bearing pluton. *Sov Geol Geofyz* 29:33–41
- Konnikov EG, Kislov EV, Orsoev DA (1994) Yoko-Dovyren layered pluton and related mineralization, northern Transbaikalia. *Geol Ore Depos* 36:545–553 (in Russian)
- Konnikov EG, Tsygankov AA, Vrublevskaya TT (1999) The Baikal–Muya volcanic-plutonic belt: lithotectonic complexes and geodynamics. GEOS, Moscow (in Russian)
- Konnikov EG, Meurer WP, Neruchev SS, Prasolov EM, Kislov EV, Orsoev DA (2000) Fluid regime of platinum group elements (PGE) and gold-bearing reef formation in the Dovyren mafic–ultramafic layered complex, Eastern Siberia, Russia. *Mineral Dep* 35:526–532
- Li C, Ripley EM (2009) Sulfur contents at sulfide-liquid or anhydrite saturation in silicate melts: empirical equations and example applications. *Econ Geol* 104:405–412
- Locmelis M, Pearson NJ, Barnes SJ, Fiorentini ML (2011) The role of chromite in the fractionation of ruthenium—new insights from in-situ laser ablation ICP-MS analysis. *Geochim Cosmochim Acta* 75:3645–3661
- Longerich HP, Jackson SE, Gunther D (1996) Laser ablation inductively coupled plasma mass spectrometric transient signal data acquisition and analyte concentration calculation. *JAAS* 11:899–904
- Manuilova MM, Zarubin VV (1981) Precambrian volcanogenic rocks of the northern Baikal region. Nauka, Leningrad (in Russian)
- Mungall JE, Brenan JM (2014) Partitioning of platinum-group elements and Au between sulfide liquid and basalt and the origins of mantle-crust fractionation of the chalcophile elements. *Geochim Cosmochim Acta* 125:265–289
- Naldrett AJ, Wilson AH (1990) Horizontal and vertical zonations in noble-metal distribution in the great dyke of Zimbabwe: a model for the origin of the PGE mineralization by fractional segregation of sulfide. *Chem Geol* 88:279–300
- Orsoev DA, Rudashevskii NS, Kretser YL, Konnikov EG (2003) Precious metal mineralization in low-sulfide ores of the Ioko–Dovyren layered massif, northern Baikal region. *Dokl Earth Sci* 390:545–549
- Page P, Barnes S-J (2013) Improved in-situ determination of PGE concentration of chromite by LA-ICP-MS: towards a better understanding. Proceedings of the 12th SGA Biennial Meeting, Uppsala, Sweden, 3:1050–1053
- Parfenov LM, Badarch G, Berzin NA et al. (2010) Chapter 1 (Introduction). In: Nokleberg WJ (ed) *Metallogenesis and tectonics of northeast Asia*. USGS Prof. Paper 1765, p 1
- Patten C, Barnes S-J, Mathez EA, Jenner FE (2013) Partition coefficients of chalcophile elements between sulfide and silicate melts and the early crystallization history of sulfide liquid: LA-ICP-MS analysis of MORB sulfide droplets. *Chem Geol* 358:170–188
- Polyakov GV, Izokh AE (2011) The prospects of expansion of the Precambrian platinumiferous province of the southern Siberian Platform. In: *Platinum of Russia*, Collection of scientific works, vol 8. Krasnoyarsk, pp 264–274 (in Russian)
- Polyakov GV, Tolstykh ND, Mekhonoshin AS, Izokh AE, Podlipkii MY, Orsoev DA, Kolotilina TB (2013) Ultramafic–mafic igneous complexes of the Precambrian East Siberian metallogenic province (southern framing of the Siberian craton): age, composition, origin, and ore potential. *Russian Geol Geophys* 54:1319–1331
- Rose LA, Brenan JM (2001) Wetting properties of Fe–Ni–Co–Cu–O–S melts against olivine: implications for sulfide melt mobility. *Econ Geol & the Bull Soc Econ Geol* 96:145–157
- Rudashevsky NS, Kretser YL, Orsoev DA, Kislov EV (2003) Palladium–platinum mineralization in copper–nickel vein ores in the Ioko–Dovyren layered massif. *Dokl Earth Sci* 391:858–861
- Rytsk EY, Shalaev VS, Rizvanova NG, Krymskii RS, Makeev AF, Rile GV (2002) The Olokit Zone of the Baikal Fold Region: new isotopic geochronological and geochemical data. *Geotectonics* 36:24–35
- Tolstykh ND, Orsoev DA, Krivenko AP, Izokh AE (2008) Noble-metal mineralization in layered ultrabasic–basic massifs of the southern Siberian platform. Parallel, Novosibirsk (in Russian)
- Wilson AH (2012) A chill sequence to the Bushveld Complex: insight into the first stage of emplacement and implications for the parental magmas. *J Petrology* 53:1123–1168
- Yaroshevsky AA, Ionov DA, Mironov YV, Koptev-Dvornikov EV, Abramov AV, Krivoplyasov GS (1982) Petrography and geochemistry of the Yoko-Dovyren dunite–troctolite–gabbro–norite layered massif, northern Baikal area. In: *Petrology and ore potential of natural rock associations*. Nauka, Moscow, pp 86–117 (in Russian)